AN ABSTRACT OF THE THESIS OF

Balamurugesh Thirunavukarasu for the degree of Master of Science in Mechanical Engineering presented on April 7, 2003.

Title: A Study of Solidification Dynamics with Liquid Mass Influx

Abstract approved: Redacted for privacy

James A Liburdy / Deborah V Pence

A computational model is developed to study the effects of alumina layer formation on an ablative surface when exposed to high temperature particle laden gas flow. The solidification dynamics i.e., the solid and liquid alumina layer growth rate, and the heat transferred to the ablative surface are investigated. A one-dimensional model is developed taking into consideration the thermal loading, particle loading and the temperature dependence of the thermo-physical properties of alumina. A fully implicit finite volume method is used to solve the coupled set of non-linear heat conduction equations. The solidification interface is tracked using the Lagrangian interpolation technique. The particle mass flux was found to be the major factor affecting the solid layer growth rate. The gas heat flux also has a major effect on the solid growth rate and the heat transferred to the ablative surface, but only for lower particle mass fluxes. On other hand the particle temperature has a linear effect on the solidification dynamics and the heat transferred to the ablative surface for all particle mass fluxes. The heat transferred to the ablative surface is reduced by approximately 39% to 88%, depending on the mass fluxes, due to the formation of the alumina layer.

A Study of Solidification Dynamics with Liquid Mass Influx

by

Balamurugesh Thirunavukarasu

A THESIS

submitted to

Oregon State University

in partial fulfillment of
the requirements for the
degree of

Master of Science

Presented April 7, 2003
Commencement June 2003

Master of Science thesis of Balamurugesh Thirunavukarasu presented on April 7, 2003

APPROVED:

Redacted for privacy

Co-Major Professor, Mechanical Engineering

Redacted for privacy

Co-Major Professor, Mechanical Engineering

Redacted for privacy

Head of Department Mechanical Engineering

Redacted for privacy

Dean of Graduate School

I understand that my thesis will become part of the permanent collection of Oregon State University libraries. My signature below authorizes release of my thesis to any reader upon request.

Redacted for privacy

Balamurugesh Thirunavukarasu, Author

ACKNOWLEDGMENTS

It is my great pleasure to thank all the people who helped me reach the stage where I am now. Of all people, I am immensely grateful to my parents, sisters and brother, who always believed in my dreams. Without their moral support, all my dreams would have never come true.

I would like to thank Dr. James Liburdy and Dr. Deborah Pence, my major advisors, for all their patience and time they invested in making this thesis successful. I am grateful to Dr. Liburdy, my philosopher and guide, for his continuous support and encouragement throughout my masters program. I would also like to thank Dr. Vinod Narayanan and Dr. Milo D Koretsky for showing interest in my research and serving as my committee members.

I would like to thank my friends Aarti, Akella, Eswar, Gokul, Kannan, Peroly, Parth, Ram, Ramesh, Venkat and Sireesha for all the fun they bought into my life and making life in Corvallis more enjoyable.

TABLE OF CONTENTS

TABLE OF CONTENTS (Continued)

TABLE OF CONTENTS (Continued)

Page

LIST OF FIGURES

LIST OF FIGURES (Continued)

Figure Page

LIST OF FIGURES (Continued)

Figure Page

LIST OF TABLES

NOMENCLATURE

A	Projected area for particle mass flux, m^2
c_p	Specific heat capacity of alumina, J/kgK
h_g	Convective heat transfer coefficient for the exhaust gas, W/m^2K
H	Latent heat of solidification of alumina, J/kg
k	Thermal conductivity of alumina, W/mK
L	Instantaneous thickness of the alumina layer, m
Li_{ref}	Initial reference length, m
$\dot{m}''_p$	Particle mass flux, kg/m^2s
$\dot{m}''_s$	Solidification rate of alumina, kg/m^2s
m_{cv}	Mass of the top control volume per unit area, kg/m^2
m_{pp}	Mass of the particle deposited in a single time step per unit area, kg/m^2
q''_{ab}	Heat flux at the ablative surface/solid alumina interface, W/m^2
q''_{gas}	Gas heat flux, W/m^2
q''_s	Heat flux at the alumina/gas interface defined by Eq. 3.15, W/m^2
$q''_{S/L}$	Heat flux at the solid/liquid alumina interface, W/m^2
q''_{KE}	Particle kinetic energy converted to thermal energy, W/m^2
$q''_{particle}$	Particle thermal energy, W/m^2
q''_{gen}	Heat released from solidification, W/m^2
s	Thickness of the solid alumina layer, m
t	Time, s
t_{ref}	Reference time, Li^2_{ref}/α_o, s

T Temperature, K

T_a Fail temperature of the ablative surface, K

T_g Temperature of the exhaust gas, K

T_i Melting temperature of alumina, K

T_p Particle temperature, K

T_s Temperature of the alumina surface, K

V_p Particle velocity, m/s

Δt Time step, s

y y-direction

Greek Symbols

α Thermal diffusivity of alumina, m^2/s

δ Non-dimensional solid alumina layer thickness

δ_l Thickness of the liquid alumina layer, m

δ_n Thickness of the deposited alumina in each time step, m

δ_s Thickness of the solid alumina layer, m

δ_s/L Relative thickness of solid alumina layer

δ_L/L Relative thickness of liquid alumina layer

$\Delta\zeta$ Non-dimensional spatial step, $\Delta y/L$

$\Delta\tau$ Non-dimensional time step, $\Delta t/t_{ref}$

ζ Non-dimensional thickness of the alumina layer, $y/L(t)$

θ Non-dimensional temperature, $(T - T_a)/(T_p - T_a)$

θ_i Non-dimensional melting temperature of alumina, $(T_i - T_a)/(T_p - T_a)$

θ_s Non-dimensional surface temperature of alumina layer, $(T_s - T_a)/(T_p - T_a)$

ρ Density of alumina, kg/m^3

τ Non-dimensional time, t/t_{ref}

Subscripts

l Liquid alumina layer

o Properties evaluated at the reference temperature

s Solid alumina layer

A STUDY OF SOLIDIFICATION DYNAMICS WITH LIQUID MASS INFLUX

1. INTRODUCTION

1.1. Background

Problems involving phase change have been studied over the past several decades numerically. In these phase change problems, the position of a moving boundary with respect to time has to be solved as an inherent part of the solution. Methods for finding this moving boundary in a fixed domain have been presented by numerous previous researchers [1]. A literature survey on problems with moving boundaries and simultaneous expanding domains showed that very little research has been done with problems dealing with both expanding domain and phase change boundary. One such problem with expanding domain and moving boundaries is studied here. In this problem the domain expands due to mass influx and an internal moving boundary is present due to phase change.

The incentive for this study is based on operation of reusable missile launchers. Missile launchers used currently consist of several launch canisters that contain missiles. When the missiles are launched from the canisters the exhaust plumes from the missile motor impose severe thermal and surface erosion on the walls of the plenum and the uptake. To protect the launchers from such severe erosions thick ablative liners are used to absorb the thermal load. The problem studied here has

already been investigated by numerous previous researchers and recently by Lewis and Anderson [2] and it is again discussed below.

To increase the performance of the missile motors, aluminum is used in the solid propellant which produces a two-phase exhaust plume consisting of molten alumina (Al_2O_3) and gaseous products of combustion. About 40% by weight of the exhaust products in some missile motors consist of aluminum in the form of alumina [2]. The alumina in the exhaust forms a thin melt layer on the ablative surface. In the early phase of the missile launch the presence of alumina particles in the exhaust plume results in a higher mechanical and thermal erosion of the ablative surface. Later, after the melt layer thickens, the alumina layer actually starts acting as a shield protecting the ablative layer from further mechanical and thermal erosion. The thermal load on the ablative layer decreases during the course of the missile launch due to the increasing thickness of the alumina layer. To incorporate design modifications to the existing missile launchers and to design future missile launchers, accurate estimates of these thermal loads during a missile launch is required. Improving the design of the existing launchers would increase the number of missiles that could be fired from a canister before refurbishing the ablative layer. Also accurate heat transfer predictions are needed in the case of missile launch failure where by the ablative layer should be able to withstand the thermal loading throughout the motor burn [2].

The formation of this alumina layer and its effects on the surface heat transfer and the degree of ablation of the ablative layer is still unresolved [2]. The problem in hand was analyzed by numerous previous researchers by making different assumptions to simplify the problem. All the models of the previous researchers either

under-predicted or over-predicted the experimental results due to assumptions made in the course of building the model.

1.2. General Problem Statement

The aim of this research is to build a numerical model that will help study the dynamics of formation of the alumina layer on the ablative surface and predict more accurately the heat transferred to the ablative surface below. The model should take into consideration the assumptions made by the previous researchers.

To study the solidification dynamics and predict the heat transfer rate to the ablative surface the following should be considered for an one-dimensional geometry:

- Thermal loading (i.e., applied surface heat flux and duration of heating)
- Particle loading (i.e., particle mass flow rate)
- Transient heat conduction and solidification of the alumina layer
- Variation of the thermo-physical properties with temperature

1.3. Present Approach

A transient, one-dimensional heat transfer prediction model that includes the combined effect of melt layer formation and solidification is developed from the principles of physics and solidification dynamics. The goal is to relate the heat transferred to the ablative surface to the parameters of the system i.e., particle mass flow rate, particle temperature, and gas heat flux. In formulating the model the variation of the thermo-physical properties with temperature is accounted for

i.e., thermal conductivity and specific heat capacity. Also the solid layer and the liquid layer are allowed to grow simultaneously and the temperature distribution in the alumina layer, including the surface temperature of the alumina layer, is explicitly solved in the model.

The flow characteristics of the exhaust gas were also investigated by Lewis and Anderson [2]. In their work it was reported that the exhaust gas forms a characteristic recirculation region, near the stagnation point, having low shear stress values inside the region. In this region the alumina will not be smeared due to the low shearing rate imposed by the exhaust gas. The computational model developed in this research will more accurately predict the effects of the alumina in this region because the model assumes that the alumina is not convected.

A FORTRAN program using the finite volume method was written to capture the physics involved and study the solidification dynamics of the alumina layer. The model uses a transformed grid to account for the mass influx and variable control volume size at the phase change interface to account for the moving boundary due to phase change. The control volume size near the solidification interface and the location of the interface is calculated using the Lagrangian interpolation technique. Due to the unavailability of experimental data, the numerical model developed was partially verified using the analytical solution of the Stefan problem. The verified numerical model is employed to study the separate effects of the various model parameters on the heat transferred to the ablative surface. With this heat transfer information, suitable design modification can be implemented to the existing ablative layers for improved performance. This information can also aid in future VLS (Vertical Launch System) designs.

2. LITERATURE REVIEW

The heat transfer predictions in missile launchers has been studied by numerous previous researchers. This section presents the work done by previous researchers and the assumptions in their models.

2.1. Previous Related Studies

Ungar [3] analyzed experimentally the effects of high velocity particle impacts on an ablating body (Micarta 259-2) by exposing it to a particle laden rocket motor plume. The rocket motor plume was seeded with aluminum oxide and glass particles and was tested separately. It was observed that the alumina particles did not melt in the rocket motor but rather fractured upon impact and were present as discrete cracked particles. On the other hand the glass particles melted before impact and were present as a thorough mix of glass and Micarta particles. He developed an equation relating the surface erosion, particle velocity, melt layer thickness, particle size and density. He assumed that a layer of molten Micarta protects the surface of the ablating body from particle impact by decelerating the incoming particles. It was also assumed that the effect of the particle impact was to transfer energy to the plastic, thus increasing the decomposition rate of the plastic filler in the Micarta 259-2. His correlation does not make any distinction between solid and liquid particles but his analysis shows that the particle impacts influence the thermal energy transfer to the ablating body.

Soo Hoo [4] numerically predicted the plenum floor erosion in the vertical launching system from a MK 104 dual-thrust rocket motor under restrained firing.

In his heat transfer model the particle kinetic energy and the gas heat flux were the only factors included. The plume and particle velocity were calculated using a fully-coupled two-phase invisid hydrocode. The model also assumes that the surface temperature of the melt layer is equal to the melt temperature of the alumina. He justifies that the particle thermal energy is important only during the initial period of launch. But once the melt layer forms, the surface temperature should nearly equal the incoming particle temperature and little additional thermal energy can be transferred. The predicted results were higher than the experimental results. Soo Hoo attributed this to the inviscid nature of the hydrocode which over-predicted the particle velocity.

Yang et. al [5], [6] developed a transient two-dimensional material erosion model to describe the simultaneous process of thermo-chemical ablation and mechanical erosion of ablative materials. The model assumes that the particles impact the ablative material and reflect off the ablative surface. The thermal energy of the particles is conducted to the ablative material only during this impact. Since the duration of the impact is very small the amount of thermal energy transferred to the ablative material is neglected. The model does not account for the formation of the melt layer on the ablative surface. The model predicts that the mechanical erosion due to particle impact is as important as erosion due to thermo-chemical ablation. The predicted results for the overall material erosion were found to agree reasonably well with the available experimental data. Unfortunately, the model does not account for the effect of the melt layer formation on the thermo-mechanical erosion of the ablative material.

Cheung et. al. [7] extended the model of Yang et. al. [5], [6] to predict the thermo-mechanical erosion of ablative materials by allowing a melt layer to form on the ablative surface. They used a combined integral and numerical technique to determine the local thickness and velocity of the melt layer from the equations of motion. The model predicts that the presence of the melt layer significantly reduces the overall erosion by slowing down the incoming particles and also increases the heat transfer resistance by acting as a shield. The model accounts for the effect of melt layer on the ablative surface but fails to consider the solidification of the melt layer that might take place within the melt layer. Experimental evidence was needed to further validate the presented theoretical results.

Lewis and Anderson [2] studied the effects of melt layer formation on the ablative materials exposed to highly aluminized rocket motor plumes. The two-phase upwind implicit finite-volume Navier-Stokes code, CRAFT [12], was used to predict the free field plume. Their model accounts for the solidification of alumina as opposed to the models developed by the previous researchers. An integral technique was used to predict the melt layer thickness and the heat transferred across the melt layer. But the melt layer thickness was assumed to have a constant thickness during the transient growth of the solid alumina layer. They assumed that the molten layer grows much faster than the solid layer and adjusts rapidly to the changes of the solid layer thickness to maintain equilibrium. The steady state thickness of the solid layer depends on the heat flux passing through the melt layer. Their model under predicts erosion by 25% on a HAVEG 41N ablative material. They suggest a better model which should take into account the simultaneous growth of solid and liquid alumina layer.

2.2. Background Literature on Moving Boundary Problems

Although an exhaustive number of methods are available for solving phase change problems, only limited number of methods has been reviewed in this section. Front tracking methodologies for solving the moving boundary problem can be categorized as fixed grid methods and modified grid methods. The following section gives the background over the various effective solution methodologies.

2.2.1. Fixed Grid Method

Crank [8] solved the moving boundary problems in diffusion and heat flow using the fixed grid method. In this method he tracked the moving boundary using the Lagrange interpolation technique which basically uses variable grid spacing at the phase change boundary. The method approximates the partial derivatives using a Lagrange interpolation formula. He proposed that at any time, $j\delta t$, the phase-change boundary will usually be located between two neighboring grid points, say $i\delta x$ and $(i+1)\delta x$ which can be tracked by using modified finite-difference formulae which incorporate unequal space intervals near the moving boundary. The general function $f(x)$ which uses known values $f(a_0), f(a_1), f(a_2)$ at three points $x = a_0, a_1, a_2$, respectively, is given by the Lagrange formula as

$$f(x) = \sum_{j=0}^{2} (l_j(x) f(a_j)) \tag{2.1}$$

where

$$l_j(x) = \frac{p_2(x)}{(x - a_j)p_2'(a_j)}, \qquad p_2(x) = (x - a_0)(x - a_1)(x - a_2)$$

and $p_2'(a_j)$ is its derivative with respect to x evaluated at $x = a_j$. It follows that

$$\frac{df}{dx} = l_0'(x)f(a_0) + l_1'(x)f(a_1) + l_2'(x)f(a_2) \tag{2.2}$$

where

$$l_0'(x) = \frac{(x - a_1)(x - a_2)}{(a_0 - a_1)(a_0 - a_2)},$$

and similarly for $l_1'(x), l_2'(x)$. Using these approximations for the partial derivatives the temperature on either side of the moving boundary is found.

2.2.2. Modified Grid Methods

Douglas and Gallie [9], instead of using a fixed time step and tracking the moving boundary, determined a variable time step as part of the solution, such that the moving boundary coincides with a grid line in space at each time level. In their method the time step was calculated by an iterative scheme which was carried out until an expression containing the rate of change of the total heat content is satisfied. But this method was prone to instability and was very sensitive to rounding errors. This method was modified by Gupta and Kumar [10] to avoid the instability caused the integral form of the boundary condition by using the finite difference form of the boundary condition.

Murray and Landis [11] used a fixed time step but variable space interval to solve the moving boundary problem in the Cartesian coordinates. They kept the number of space intervals in the solid and liquid region constant so that the space intervals increase in the solid region at the same time in the liquid region the space intervals decrease as the solidification takes place. Thus the moving front will

always be located on the same grid point throughout the solution. To start the solution there should be both solid and liquid regions present and should be of finite thickness. They assumed a starting solution but they suggest that any error in the starting solution would decay as the solution proceeds.

3. DEVELOPMENT OF PHYSICAL AND MATHEMATICAL MODEL

When the ablative layer is exposed to a high temperature particle laden gas flow, a melt layer starts developing on the surface of the ablative layer. As the melt layer cools solidification of the alumina occurs near the ablative surface. So there exits an outer moving boundary due to the particle mass influx which has an inner moving boundary due to the solidification of alumina. To facilitate mathematical formulation of the heat transfer problem, the following simplifying assumptions are employed:

1. The fail temperature of the ablative layer (1600 K) is reached instantly and remains constant, as supported by experiments.

2. The effect of the shear stress due to the exhaust gas on the top of the melt layer is neglected.

3. There are no advection effects due to the pyrolysis gases from the ablative layer.

4. The solid/liquid interface temperature is at 2327 K (melting temperature of alumina) i.e. a fixed interface temperature and there is no mushy region.

5. The kinetic energy of the particles is fully converted into thermal energy.

6. The ablative surface is exposed to a constant average particle mass flow rate.

7. The decomposition of the ablative layer does not affect the heat transfer process.

8. The gas phase applies a constant heat flux on the surface of the melt layer.

9. The process of heat transfer can be treated as transient and one-dimensional.

Figure 3.1 shows a schematic of the ablative layer exposed to a particle laden gas flow. Since the mass flow rate of the alumina particles is assumed to be a constant, at any given time the amount of alumina deposited on the ablative layer is given as

$$\delta_n = \frac{\dot{m}_p \Delta t}{\rho} \tag{3.1}$$

where

$\delta_n \equiv$ thickness of the alumina deposited on the ablative surface in time Δt

$\dot{m}_p \equiv$ mass flux of alumina particles

$\rho \equiv$ density of alumina

$\Delta t \equiv$ time step

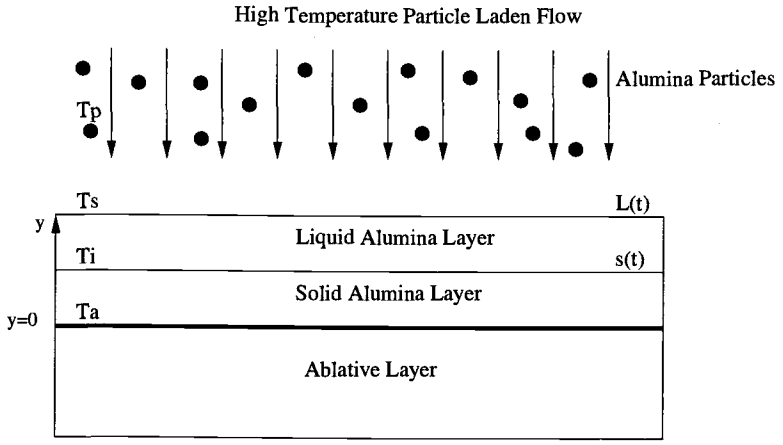

Figure 3.1. Schematic of ablative layer exposed to a particle laden flow.

3.1. Energy Balance

The deposited particles have thermal and kinetic energy associated with them which is released upon impingement on the surface. Also the plume gas is assumed to impose a constant heat flux on the exposed surface. The pressure work is negligible because of small alumina layer growth rate. So energy is nearly equal to enthalpy. Figure 3.2 shows the various forms of energy addition and removal from the alumina layer. Equation 3.2 gives an overall energy balance for the alumina layer.

$$\dot{E}_{in} + \dot{E}_{gen} = \dot{E}_{out} + \dot{E}_{st} \tag{3.2}$$

where

$\dot{E}_{in} \equiv$ net rate of heat input

$\dot{E}_{gen} \equiv$ net rate of heat generation

$\dot{E}_{out} \equiv$ net rate of heat transfer out

$\dot{E}_{st} \equiv$ net rate of internal energy change

Each term in Eq. 3.2 can be represented as follows:

Net Rate of Heat Input, $\dot{E}_{in}$

The net rate of heat input,$\dot{E}_{in}$, includes three components, i.e., the energy from the exhaust gas $\dot{q}_{gas}$, the thermal energy released by the particles $\dot{q}_{particle}$ and the kinetic energy of the particles $\dot{q}_{KE}$.

$$\dot{E}_{in} = \dot{q}_{KE} + \dot{q}_{gas} + \dot{q}_{particle} \tag{3.3}$$

Based on the assumption that the particles upon impinging the alumina surface

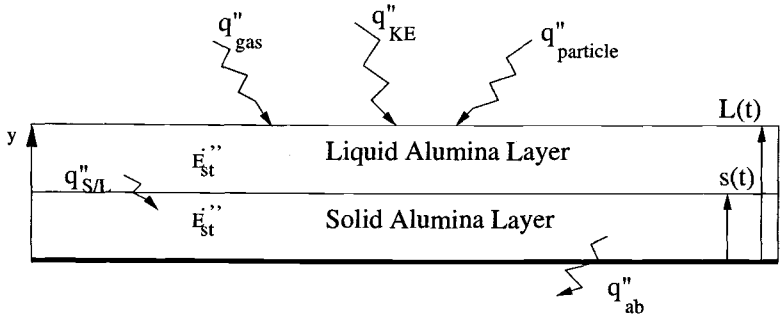

Figure 3.2. Energy balance for the alumina layer.

loose all their kinetic energy by converting the kinetic energy to thermal energy, then

$$\dot{q}_{KE} = \frac{1}{2}\dot{m}_p V_p^2 A \tag{3.4}$$

where

$V_p \equiv$ average particle velocity

$A \equiv$ projected area for mass influx

The exhaust gas from the rocket motor is assumed to impose a constant heat flux on the alumina surface which is given as:

$$\dot{q}_{gas} = h_g A(T_g - T_s) = -kA\left(\frac{\partial T}{\partial y}\right)_{y=L} \tag{3.5}$$

where

$h_g \equiv$ convective heat transfer coefficient

$k \equiv$ thermal conductivity of alumina

$T_g \equiv$ exhaust gas temperature

$T_s \equiv$ surface temperature of the alumina layer

It is assumed that the particles release their thermal energy upon impingement and cool down to an average surface temperature, T_{avg}. The particles are assumed to releases all their thermal energy as soon as they enter the melt layer and hence the energy is directly added to the surface of the melt layer. The details of the manner in which the particle thermal energy is accounted for in the model is discussed in the Chapter 4. The particle thermal energy is given by

$$\dot{q}_{particle} = \dot{m}_p c_p A(T_p - T_{avg}) \tag{3.6}$$

where

$T_p \equiv$ temperature of the particles

$c_p \equiv$ specific heat capacity of the alumina

Net Rate of Heat Generation, $\dot{E}_{gen}$

The net rate of heat generation, $\dot{E}_{gen}$, represents the thermal energy released from the phase change of alumina which is given as:

$$\dot{E}_{gen} = \rho A H \frac{\partial s}{\partial t} \tag{3.7}$$

where

$H \equiv$ latent heat of solidification for alumina

$\frac{\partial s}{\partial t} \equiv$ velocity with which the solidification front moves

Net Rate of Heat Transfer Out, $\dot{E}_{out}$

The net rate of heat transfer out, $\dot{E}_{out}$, represents the heat conducted to the ablative surface which is given as:

$$\dot{E}_{out} = -k_s A \left(\frac{\partial T}{\partial y}\right)_{y=0} \tag{3.8}$$

Net Rate of Internal Energy Change, $\dot{E}_{st}$

The net rate of internal energy change, $\dot{E}_{st}$, represents the rate at which thermal energy is stored in the alumina layer. Changes in potential and kinetic energy of the total layer are assumed negligible. This is given as:

$$\dot{E}_{st} = \int_0^L \rho A c_p \frac{\partial T}{\partial t}\, dy \tag{3.9}$$

where $L(t)$ represents instantaneous thickness of the alumina layer.

3.2. Governing Equations

The temperature distribution in the deposited alumina layer, considering both the solid(s) and liquid(l) layers, is governed by the transient one dimensional heat conduction equation [1]:

$$\rho_s c_{ps} \frac{\partial T_s}{\partial t} = \frac{\partial}{\partial y}\left(k_s \frac{\partial T_s}{\partial y}\right) \qquad 0 \le y \le s(t) \tag{3.10}$$

$$\rho_l c_{pl} \frac{\partial T_l}{\partial t} = \frac{\partial}{\partial y}\left(k_l \frac{\partial T_l}{\partial y}\right) \qquad s(t) \le y \le L(t) \tag{3.11}$$

where

$s(t) \equiv$ location of the solid/liquid alumina interface

$L(t) \equiv$ location of the liquid alumina/gas interface

$k_l \equiv$ thermal conductivity of liquid alumina

$k_s \equiv$ thermal conductivity of solid alumina

$c_{pl} \equiv$ specific heat capacity of liquid alumina

$c_{ps} \equiv$ specific heat capacity of solid alumina

3.2.1. Initial and Boundary Condition

In order to solve the transient one-dimensional governing equations, a set of initial and boundary conditions must be specified. The initial condition assumes the presence of a very thin layer of alumina on the ablative surface which is initially at a temperature equal to the fail temperature of the ablative layer:

$$T(y,0) = T_a \tag{3.12}$$

where T_a is the fail temperature of the ablative layer.

The alumina layer is subjected to a constant temperature boundary condition equal to the fail temperature of the ablative layer at the ablative surface/solid alumina interface given by:

$$T(0,t) = T_a \tag{3.13}$$

At the top surface, i.e. the gas/liquid alumina interface, a constant heat flux boundary condition is applied which is given by:

$$-k\left(\frac{\partial T}{\partial y}\right)_{y=L} = \dot{q_s''} \tag{3.14}$$

where $\dot{q_s''}$ is the constant surface heat flux defined by Eq. 3.15 or 3.17. The magnitude of this surface heat flux is affected by different factors depending on whether the alumina layer is in the early phase or late phase of development, described below.

3.2.1.1. Alumina Layer in the Early Phase

The early phase of alumina layer development can be defined as the phase of development in which nearly instantaneous solidification of alumina occurs due

to the large temperature difference between the incoming alumina particles and the surface temperature of the alumina layer and hence only the solid alumina layer exists. Due to this near instantaneous solidification the latent heat released from solidification of alumina, the gas heat flux $\dot{q}''_{gas}$ and the kinetic energy $\dot{q}''_{KE}$ of the particles sum to equal the constant surface heat flux $\dot{q}''_{s}$ boundary condition.

$$\dot{q}''_{s} = \dot{q}''_{gas} + \dot{q}''_{KE} + \rho H \frac{\partial L}{\partial t} \tag{3.15}$$

where

$H \equiv$ latent heat of solidification for alumina

$\dot{q}''_{gas} \equiv$ constant gas heat flux

$\dot{q}''_{KE} \equiv$ kinetic energy from the particle impingement

$\frac{\partial L}{\partial t} \equiv$ velocity with which alumina/gas interface moves due to mass influx

3.2.1.2. Alumina Layer in the Late Phase

The late phase of alumina layer development can be defined as the phase of development in which the surface temperature of the alumina layer rises above the melting temperature of alumina so that both solid and liquid alumina layers co-exist. With the solid and liquid alumina layer growing simultaneously the Stefan condition should be satisfied at the solid/liquid alumina interface. The Stefan condition is given as:

$$-k_s \left(\frac{\partial T}{\partial y}\right)_s + k_l \left(\frac{\partial T}{\partial y}\right)_l = -\rho H \frac{\partial s}{\partial t} \qquad at \quad y = s(t) \tag{3.16}$$

The heat flux boundary condition at the alumina/gas interface, q''_s, for the late phase includes only the gas heat flux $\dot{q}''_{gas}$ and the kinetic energy $\dot{q}''_{KE}$ of the

particles and is given by:

$$\dot{q}''_s = \dot{q}''_{gas} + \dot{q}''_{KE} \tag{3.17}$$

Since the particle thermal energy is released after the particles enter the melt layer, the thermal energy of the particles is directly added to the melt layer and hence not included as a boundary condition.

The governing equations 3.10 and 3.11 with initial condition 3.12 and boundary conditions 3.13 and 3.14 are solved simultaneously with the interface energy balance equation 3.16 to determine the temperature distribution in the alumina layer and the heat transfer rate to the ablative surface.

3.2.2. Non-dimensionalization

Prior to formulating the finite volume equations, the coordinate system is transformed from y and t coordinate to the corresponding dimensionless variables ζ and τ coordinate system. This can be done by setting

$$\zeta = \frac{y}{L(t)} \tag{3.18}$$

$$\tau = \frac{t}{t_{ref}} \tag{3.19}$$

$$\theta = \frac{T - T_a}{T_p - T_a} \tag{3.20}$$

where $L(t)$ is the instantaneous thickness of the alumina layer and t_{ref} is the reference time, defined below. The temperature is non-dimensionalized using the ablative surface temperature T_a and the particle temperature T_p.

Using a continuous function for the variation of the thermo-physical properties of alumina helps to combine the two governing equations Eqs. 3.10 and 3.11, into one equation. The details of the continuous function for the thermo-physical properties are discussed in Chapter 4. Using Eqs. 3.18 - 3.20 in the governing Eqs. 3.10 and 3.11 along with a continuous function for the thermo-physical properties, results in:

$$\frac{\partial \theta}{\partial \tau} = \frac{\alpha}{\alpha_o}\frac{Li_{ref}^2}{L^2}\frac{\partial^2 \theta}{\partial \zeta^2} + \frac{1}{L}\frac{dL}{d\tau}\left[\frac{\partial \zeta \theta}{\partial \zeta} - \theta\right] \qquad 0 \leq \zeta \leq 1 \tag{3.21}$$

where

$t_{ref} = \frac{Li_{ref}^2}{\alpha_o}$,

$Li_{ref} \equiv$ thickness of the alumina layer at a given fixed time

$\alpha \equiv$ temperature dependent thermal diffusivity of alumina

$\alpha_o \equiv$ thermal diffusivity at the reference temperature

$\delta = \frac{s(t)}{L(t)} \equiv$ non-dimensional solid layer thickness

Non-dimensionalized Initial and Boundary Conditions

The initial condition 3.12 and the boundary conditions 3.13 and 3.14 in the dimensionless form can written as

$$\theta(\zeta, 0) = 0 \tag{3.22}$$

$$\theta(0, \tau) = 0 \tag{3.23}$$

$$-\frac{k}{k_o}\left(\frac{\partial \theta}{\partial \zeta}\right)_{\zeta=1} = \frac{\dot{q''}_s L}{k_o(T_p - T_a)} \tag{3.24}$$

where $\dot{q}_s''$ will take the form of Eq. 3.15 or Eq. 3.17, depending on whether the alumina layer is in the early phase of development or in the late phase of development.

The dimensionless form of the Stefan condition provided in Eq. 3.16 can be rewritten as:

$$-\frac{k_s}{k_o}\left(\frac{\partial\theta}{\partial\zeta}\right)_s+\frac{k_l}{k_o}\left(\frac{\partial\theta}{\partial\zeta}\right)_l=-\frac{HL^2}{c_{po}Li_{ref}^2(T_p-T_a)}\frac{\partial\delta}{\partial\tau}\qquad at\quad \zeta=\delta \tag{3.25}$$

These non-dimensionalized Eqs. 3.21- 3.24 are used in developing the finite volume equations. Developing the finite volume equations will be discussed in development of the computational model in Chapter 4.

4. DEVELOPMENT OF COMPUTATIONAL MODEL

In the development of the computational model special attention is given to the following items:

- Expansion of the solution domain due to the mass influx
- Tracking the solid/liquid alumina interface
- Temperature dependence of the thermo-physical properties of alumina

These three concerns are addressed in the development of the model and are discussed below along with the general form of the model.

4.1. Discretization Methods

In general, to solve the governing differential equations numerically, the calculation domain must be divided into a finite number of locations (called grid points) where the unknown values of the dependent variable are calculated. The whole idea involves the task of providing a set of algebraic equations for these unknowns at the grid points and prescribing an algorithm for solving the equations. These algebraic equations are called discretization equations and the method of formulating these discretization equations can be grouped as [14]:

- Taylor-series formulation
- Variational formulation
- Method of weighted residuals and
- Control volume formulation

Taylor-series Formulation

The Taylor-series formulation, also called the finite difference method, is based on the Taylor series expansion. In this method the derivatives of the differential equations are formed by truncating the higher order terms in the Taylor series expansion. This method assumes that the higher order derivatives are unimportant and are neglected in the formulation. This method is relatively simple method, but fails to provide the physical meaning of the terms [14].

Variational Formulation

The variational formulation method is based on the calculus of variations. The basic idea of solving a differential equation is to minimize its functional. This is called the variational principle and if the functional is minimized with respect to the grid point values of the dependent variable, it results in the required discretization equations. This method is commonly used in the finite element methods for stress analysis. The method is algebraically and conceptually complex. Also this method has limited applicability in solving engineering problems, since a variational principle does not exist for all differential equations [14].

Method of Weighted Residuals

The method of weighted residuals is a very powerful method for solving differential equations. For example, consider the differential equation represented by

$$K(\psi) = 0$$

For this equation let $\bar{\psi}$ be an approximate solution, which contains an unknown parameters, x, and is given by:

$$\bar{\psi} = a_0 + a_1 x + a_2 x^2 + ... + a_m x^m$$

where the coefficients a_i are also unknown. Using $\bar{\psi}$ in the differential equation will leave a residual R defined as

$$K(\bar{\psi}) = R$$

This residual should be made as small as possible. One way of doing this is to integrate the residual over the domain of interest along with a weighting function, W,

$$\int W R \, dx = 0$$

The choice of the weighting function will generate different discretization methods. Instead of having a single approximate solution $\bar{\psi}$ that satisfies the entire domain, a piecewise profile can be used with the grid point values as unknown. One such method is the finite element method which uses piecewise profiles and the Galerkin method for the weighted residual function. The simplest weighting function is $W = 1$. Using this weighting function along with the piecewise profile results in a formulation identical to the control volume formulation [14], which is used in developing the present numerical model and is discussed in the next section.

Control Volume Formulation

In the control volume formulation, also called the finite volume method, the calculation domain is divided into a number of control volumes. Each control volume surrounds a grid point. Note that it is not necessary for the grid point to be located

at the center of the control volume. The differential equation is integrated over each control volume using a weighting function, defined in the method of weighted residuals, of unity. For this integration a piecewise profile is assumed between grid points for the unknown parameter ψ. The result is the discretization equation containing the values of ψ for a group of grid points. The advantage of the control volume method is the integral conservation of mass, momentum and energy over the control volumes and also over the entire calculation domain, which is true for any number of grid points. Thus a coarse grid solution also exhibits exact integral balances like the refined grid solution. Also the terms in the control volume formulation give a good physical meaning of what they represent in the discretized equations. The choice of the profile between grid points is arbitrary in the sense that even higher order polynomials or a stepwise profile can be used [14]. But the linear profile, being the simplest, is used in developing the numerical model in this study.

4.2. Mass Influx

The alumina layer that forms on the ablative surface grows with time due to the liquid mass influx. Due to this alumina layer growth, the solution domain should also expand to account for the mass influx during each time step. Two such methods by which the liquid mass influx can be accounted for are explained.

Expanding Grid Structure

To account for the expanding solution domain, the grid structure should also expand at the same rate as the particle mass influx. The grid structure can be expanded by either of two methods:

1. As the solution domain increases the number of control volumes can also be increased. Throughout most of the domain, the size of the control volume is a constant, yet the size of the control volume nearest to the top surface will be variable, depending on the mass flux rate and time step.

2. As the solution domain increases the number of control volumes is kept fixed but the size of each of the control volumes increase to account for the expanding solution domain.

In developing the numerical model a fixed number of control volumes with increasing size is used. This method is used for its reduced computational time and storage compared to the other method. In the equivalent y coordinate the thickness of the alumina layer increases with time and accounts for the mass influx by increasing the size of the control volumes. But in the dimensionless ζ coordinate the thickness of the alumina layer at any time is equal to unity. Employing a constant number of control volumes yields a non-dimensional spatial step size that is constant throughout the solution domain and independent of time. One way to do this is by applying a suitable coordinate transformation. Using the dimensionless coordinate ζ, which was defined in Chapter 3, by Eq. 3.18, as: $\zeta = y/L(t)$, allows the non-dimensional thickness of the alumina layer to vary from 0 to 1. Thus the coordinate transformation helps to convert the expanding domain problem into a fixed domain problem.

4.3. Descretized Equations

The discretization equations for the numerical model are derived based on the control volume formulation discussed in Section 4.1. To derive the discretization equations for the numerical model, consider the grid points shown in Fig. 4.1. P represents the grid point for which the discretization equations are derived. Since the numerical model is one-dimensional, grid point P has only two neighboring grid points, W and E, the west and east neighboring grid points, respectively. It is also assumed that the thickness of the control volume along the x and z axes is unity. The dashed lines represent the control volume faces which are denoted by e and w, the east and west control volume faces, respectively. Thus the volume of the control volume is $\Delta\zeta$ x 1 x 1, where $\Delta\zeta$ is the non-dimensional distance between faces w and e.

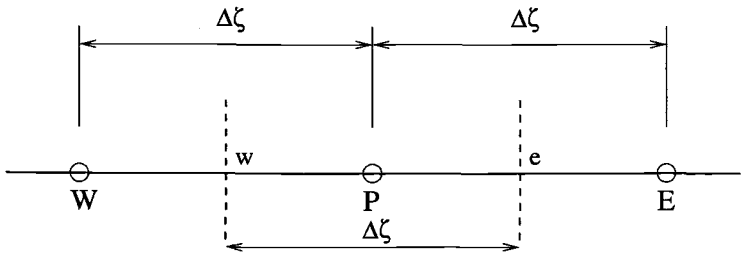

Figure 4.1. Schematic of the grid points for the one-dimensional model.

In developing the numerical model a piecewise linear profile, as shown in Fig. 4.2, is used. For this profile assumption, linear interpolation is used between grid points. Since time is a one-way coordinate, the solution can be obtained by

marching in time from a given initial temperature distribution. The discretized equation is derived by integrating the non-dimensional governing equation, Eq. 3.21, over the control volume shown in Fig. 4.1 and over the dimensionless time interval from τ to $\tau + \Delta\tau$ [13]. Thus

$$\int_w^e \int_\tau^{\tau+\Delta\tau} \frac{\rho c_p}{\rho_o c_{po}} \frac{\partial\theta}{\partial\tau}\, d\tau\, d\zeta = \frac{Li_{ref}^2}{L^2} \int_\tau^{\tau+\Delta\tau} \int_w^e \frac{k}{k_o} \frac{\partial^2\theta}{\partial\zeta^2}\, d\zeta\, d\tau +$$

$$\frac{1}{L}\frac{dL}{d\tau} \int_\tau^{\tau+\Delta\tau} \int_w^e \frac{\rho c_p}{\rho_o c_{po}} \left[\frac{\partial\zeta\theta}{\partial\zeta} - \theta\right] d\zeta\, d\tau \tag{4.1}$$

where the order of integration is chosen based on the nature of the terms.

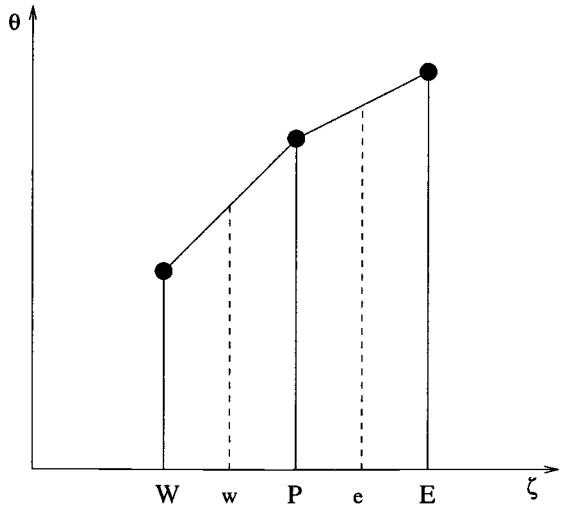

Figure 4.2. Piecewise linear profile.

If the temperature of the grid point is assumed uniform over the entire control volume, the left hand side of Eq. 4.1 can be simplified as

$$\int_w^e \int_\tau^{\tau+\Delta\tau} \frac{\rho c_p}{\rho_o c_{po}} \frac{\partial\theta}{\partial\tau}\, d\tau\, d\zeta = \frac{\rho c_p}{\rho_o c_{po}}(\theta_P - \theta_P^o)\Delta\zeta \tag{4.2}$$

In Eq. 4.2, θ_P^o represents the non-dimensional temperature at non-dimensional time τ. The first term on the right hand side of Eq. 4.1 can be simplified based on the piecewise linear profile as

$$\frac{Li_{ref}^2}{L^2} \int_\tau^{\tau+\Delta\tau} \int_w^e \frac{k}{k_o} \frac{\partial^2\theta}{\partial\zeta^2}\, d\zeta\, d\tau = \frac{Li_{ref}^2}{L^2} \int_\tau^{\tau+\Delta\tau} \left[\frac{k_e}{k_o}\frac{\theta_E - \theta_P}{\Delta\zeta} - \frac{k_w}{k_o}\frac{\theta_P - \theta_W}{\Delta\zeta}\right] d\tau \tag{4.3}$$

Similarly the second term on the right hand side of Eq. 4.1 can be simplified as

$$\frac{1}{L}\frac{dL}{d\tau} \int_\tau^{\tau+\Delta\tau} \int_w^e \frac{\rho c_p}{\rho_o c_{po}} \left[\frac{\partial\zeta\theta}{\partial\zeta} - \theta\right] d\zeta\, d\tau =$$

$$\frac{1}{L}\frac{dL}{d\tau} \int_\tau^{\tau+\Delta\tau} \left[\frac{\rho c_p}{\rho_o c_{po}}\frac{(\zeta\theta)_E + (\zeta\theta)_P}{2} - \frac{\rho c_p}{\rho_o c_{po}}\frac{(\zeta\theta)_P + (\zeta\theta)_W}{2} - \frac{\rho c_p}{\rho_o c_{po}}\theta_P\Delta\zeta\right] d\tau \tag{4.4}$$

To evaluate the Eqs. 4.3 and 4.4 an assumption should be made about the variation of $\theta_P, \theta_E, \theta_W$ with respect to time from τ to $\tau + \Delta\tau$. A general approach is to define a weighting parameter f which varies between 0 and 1. The integral can be defined as [13]:

$$\int_\tau^{\tau+\Delta\tau} \theta_P\, d\tau = [f\theta_P + (1-f)\theta_P^o]\ \Delta\tau \tag{4.5}$$

The choice of the value for the weighting factor f will result in different schemes i.e. for

- $f = 0$: Explicit scheme

- $f = 0.5$: Crank-Nicolson scheme
- $f = 1$: Fully implicit scheme

Of all the schemes the fully implicit scheme is simple, unconditionally stable and gives a physically realistic, although not accurate, solution even at large time steps. Hence the fully implicit scheme is used in developing the numerical model, with time step chosen to assume an accurate solution. Thus, using $f = 1$ gives the final form of the discretized equation as:

$$\frac{\rho c_p}{\rho_o c_{po}}(\theta_P - \theta_P^o)\frac{\Delta\zeta}{\Delta\tau} = \frac{Li_{ref}^2}{L^2}\left[\frac{k_e}{k_o}\frac{\theta_E - \theta_P}{\Delta\zeta} - \frac{k_w}{k_o}\frac{\theta_P - \theta_W}{\Delta\zeta}\right] +$$

$$\frac{1}{L}\frac{dL}{d\tau}\left[\frac{\rho c_p}{\rho_o c_{po}}\frac{(\zeta\theta)_E + (\zeta\theta)_P}{2} - \frac{\rho c_p}{\rho_o c_{po}}\frac{(\zeta\theta)_P + (\zeta\theta)_W}{2} - \frac{\rho c_p}{\rho_o c_{po}}\theta_P\Delta\zeta\right] \tag{4.6}$$

It is very helpful to write Eq. 4.6 in a standard form as given below [13]:

$$a_P\theta_P = a_E\theta_E + a_W\theta_W + b \tag{4.7}$$

where

$$a_E = \frac{Li_{ref}^2}{L^2}\frac{k_e}{k_o\Delta\zeta} + \frac{1}{L}\frac{dL}{d\tau}\frac{\rho c_p}{\rho_o c_{po}}\frac{\zeta_E}{2} \tag{4.8a}$$

$$a_W = \frac{Li_{ref}^2}{L^2}\frac{k_w}{k_o\Delta\zeta} - \frac{1}{L}\frac{dL}{d\tau}\frac{\rho c_p}{\rho_o c_{po}}\frac{\zeta_W}{2} \tag{4.8b}$$

$$a_P^o = \frac{\rho c_p}{\rho_o c_{po}}\frac{\Delta\zeta}{\Delta\tau} \tag{4.8c}$$

$$b = a_P^o\theta_P^o + S_u \tag{4.8d}$$

$$a_P = \frac{Li_{ref}^2}{L^2}\frac{k_e}{k_o\Delta\zeta} + \frac{Li_{ref}^2}{L^2}\frac{k_w}{k_o\Delta\zeta} + \frac{1}{L}\frac{dL}{d\tau}\frac{\rho c_p}{\rho_o c_{po}}\Delta\zeta + a_P^o - S_P \tag{4.8e}$$

$$S_P = 0 \tag{4.8f}$$

$$S_u = 0 \tag{4.8g}$$

where S_u and S_P represents the source terms which are used to account for boundary conditions. The values of S_u and S_P are assigned based on the source model $S = S_u + S_P\theta_P$ [13]. It is zero every where in the calculation domain except at the boundaries and the solid/liquid interface.

Evaluation of Variable Thermal Conductivity

In Eqs. 4.6 and 4.7 the thermal conductivities k_e and k_w are evaluated at the control volume faces e and w respectively. But the temperature dependence of the conductivity leads to a conductivity variation in response to the temperature distribution. A suitable function is developed to account for the temperature dependence of the thermal conductivity. Details of this function are discussed in Section 4.6. Using this function the thermal conductivity is evaluated at each grid point and the grid point thermal conductivity is used to evaluated the thermal conductivity at the control volume faces. A simple and straightforward procedure is to use the arithmetic mean. But due to disadvantages associated with the arithmetic mean in handling variable control volumes, a much better procedure, called the harmonic mean, will be used to evaluate the thermal conductivities at the control volume faces. In Fig. 4.3 the conductivity k_e at the control volume faces is required which

can be evaluated using the form [14]

$$k_e = \left(\frac{1 - f_e}{k_P} + \frac{f_e}{k_E} \right)^{-1} \tag{4.9}$$

where the factor f_e is defined as the ratio of the distances shown in Fig. 4.3 as:

$$f_e = \frac{\Delta\zeta_+}{\Delta\zeta} \tag{4.10}$$

In Eq. 4.9, k_P and k_E are the thermal conductivities evaluated at the grid points

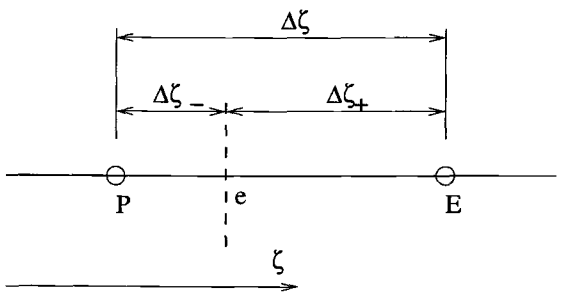

Figure 4.3. Distance associated with the control volume face e.

and k_e is the conductivity at the control volume face e. When the control volume face e is located equi-distant from P and E grid points, $f_e = 0.5$; and Eq. 4.9 reduces to

$$k_e = \frac{2k_P k_E}{k_P + k_E} \tag{4.11}$$

A similar expression for k_w can also be developed.

Equation 4.7, with coefficients defined by Eq. 4.8, represents the general discretized equation for all the internal control volumes shown in Fig. 4.4, less the

boundary control volumes WW and EE. The discretized equation that accounts for the boundary conditions are derived next.

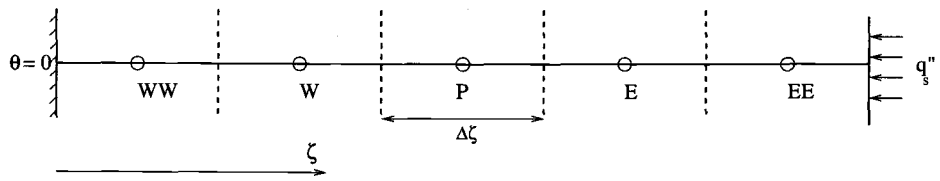

Figure 4.4. Control Volume for Internal and Boundary Grid Points.

4.3.1. Boundary Conditions

4.3.1.1. Constant Temperature Boundary Condition

As discussed in Chapter 3 a constant temperature boundary condition (Eq. 3.23) is applied at $\zeta = 0$, as shown in Fig. 4.4, where the temperature is prescribed at the left boundary of control volume WW. Integrating the non-dimensional governing Eq. 3.21 over the control volume WW and applying the boundary condition at $\zeta = 0$ we get

$$\frac{\rho c_p}{\rho_o c_{po}}(\theta_P - \theta_P^o)\frac{\Delta\zeta}{\Delta\tau} = \frac{L i_{ref}^2}{L^2}\left[\frac{k_e}{k_o}\frac{\theta_E - \theta_P}{\Delta\zeta} - \frac{k_w}{k_o}\frac{\theta_P}{\Delta\zeta/2}\right] +$$

$$\frac{1}{L}\frac{dL}{d\tau}\left[\frac{\rho c_p}{\rho_o c_{po}}\frac{(\zeta\theta)_E + (\zeta\theta)_P}{2} - \frac{\rho c_p}{\rho_o c_{po}}\theta_P \Delta\zeta\right] \qquad (4.12)$$

Equation 4.12 can be written in a more generalized and useful form [13]

$$a_P\theta_P = a_E\theta_E + a_W\theta_W + b \tag{4.13}$$

where

$$a_E = \frac{Li_{ref}^2}{L^2}\frac{k_e}{k_o\Delta\zeta} + \frac{1}{L}\frac{dL}{d\tau}\frac{\rho c_p}{\rho_o c_{po}}\frac{\zeta_E}{2} \tag{4.14a}$$

$$a_W = 0 \tag{4.14b}$$

$$a_P^o = \frac{\rho c_p}{\rho_o c_{po}}\frac{\Delta\zeta}{\Delta\tau} \tag{4.14c}$$

$$b = a_P^o\theta_P^o + S_u \tag{4.14d}$$

$$a_P = \frac{Li_{ref}^2}{L^2}\frac{k_e}{k_o\Delta\zeta} + \frac{1}{L}\frac{dL}{d\tau}\frac{\rho c_p}{\rho_o c_{po}}\zeta_P + \frac{1}{L}\frac{dL}{d\tau}\frac{\rho c_p}{\rho_o c_{po}}\Delta\zeta + a_P^o - S_P \tag{4.14e}$$

$$S_P = -\frac{k_w}{k_o}\frac{1}{\Delta\zeta/2} \tag{4.14f}$$

$$S_u = 0 \tag{4.14g}$$

In the control volume approach the source terms are used to account for boundary conditions based on the source term model $S = S_u + S_P\theta_P$ [13]. The value of S_u and S_P in Eq. 4.14 are identified based on this model.

4.3.1.2. Constant Heat Flux Boundary Condition

As discussed in Chapter 3 a constant heat flux boundary condition (Eq. 3.24) is applied at $\zeta = 1$, as shown in Fig. 4.4, where the heat flux is prescribed at the right boundary of the control volume EE. Integrating the non-dimensional governing Eq. 3.21 over the control volume EE and applying the boundary condition at $\zeta = 1$ result in

$$\frac{\rho c_p}{\rho_o c_{po}}(\theta_P - \theta_P^o)\frac{\Delta\zeta}{\Delta\tau} = \frac{Li_{ref}^2}{L^2}\left[\frac{\dot{q}''_S L}{k_o(T_p - T_a)} - \frac{k_w}{k_o}\frac{\theta_P - \theta_W}{\Delta\zeta}\right] +$$

$$\frac{1}{L}\frac{dL}{d\tau}\left[\frac{\rho c_p}{\rho_o c_{po}}\theta_S - \frac{\rho c_p}{\rho_o c_{po}}\frac{(\zeta\theta)_P + (\zeta\theta)_W}{2} - \frac{\rho c_p}{\rho_o c_{po}}\theta_P\Delta\zeta\right] \tag{4.15}$$

where θ_S is the extrapolated alumina layer surface temperature.

Equation 4.15 can be written in a more generalized and useful form [13] as

$$a_P\theta_P = a_E\theta_E + a_W\theta_W + b \tag{4.16}$$

where

$$a_E = 0 \tag{4.17a}$$

$$a_W = \frac{Li_{ref}^2}{L^2}\frac{k_w}{k_o\Delta\zeta} - \frac{1}{L}\frac{dL}{d\tau}\frac{\rho c_p}{\rho_o c_{po}}\frac{\zeta_W}{2} \tag{4.17b}$$

$$a_P^o = \frac{\rho c_p}{\rho_o c_{po}}\frac{\Delta\zeta}{\Delta\tau} \tag{4.17c}$$

$$b = a_P^o\theta_P^o + Su \tag{4.17d}$$

$$a_P = \frac{Li_{ref}^2}{L^2}\frac{k_w}{k_o\Delta\zeta} + \frac{1}{L}\frac{dL}{d\tau}\frac{\rho c_p}{\rho_o c_{po}}\zeta_P + \frac{1}{L}\frac{dL}{d\tau}\frac{\rho c_p}{\rho_o c_{po}}\Delta\zeta + a_P^o - S_P \tag{4.17e}$$

$$S_P = 0 \tag{4.17f}$$

$$S_u = \frac{Li_{ref}^2}{L^2}\frac{\dot{q}''_S L}{k_o(T_p - T_a)} + \frac{1}{L}\frac{dL}{d\tau}\frac{\rho c_p}{\rho_o c_{po}}\theta_S \tag{4.17g}$$

The values of S_u and S_P are assigned based on the source term model $S = S_u + S_P\theta_P$ [13].

4.3.2. Interface Condition

When the alumina layer enters the late phase of development, simultaneous growth of the solid and liquid alumina layers take place. To account for the solidification of alumina the Stefan condition, Eq. 3.25 should be satisfied at the solid/liquid alumina interface [1]. In developing the numerical model it is always ensured that the solidification front is between two adjacent grid points. This is done under the assumption that the solidification takes place at a single, finite temperature without the presence of a mushy region. Since the solidification front should always be between two adjacent grid points, the control volumes adjacent to the interface i are variable in size, as shown in Fig. 4.5. In Fig. 4.5, p represents the location of the solidification interface i from the reference grid point $r-1$, similarly i_- and i_+ represent the location of the solidification interface i from the grid points r and $r+1$, respectively.

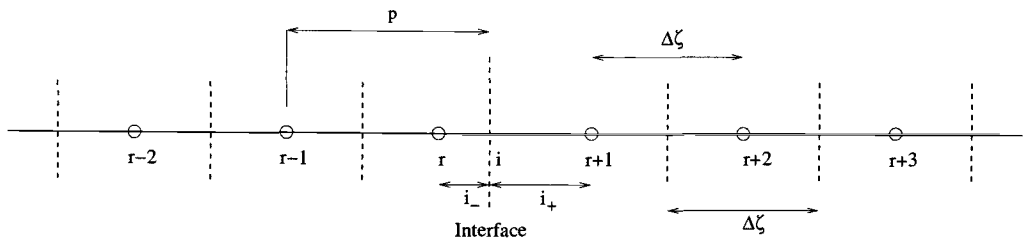

Figure 4.5. Variable control volumes near the solid/liquid interface.

Lagrange Interpolation Method

A suitable method should be used to find the location of the interface i in each time step. The Lagrange interpolation method suggested by Crank [8] is used in this numerical model to track the solidification interface i. Based on the location of the interface the size of the variable control volumes can be calculated. Figure 4.5 shows the location of the solid/liquid interface at any time τ. The interface as shown in Fig. 4.5 is located between the grid points r and $r+1$ and its location can be written as $i = (r - 1 + p)\Delta\zeta$, where p is a fraction $(1 < p < 2)$ used to track the interface location. The size of the control volumes r and $r+1$ are calculated based on the location of the solid/liquid interface. As alumina solidifies the interface moves from grid point r to $r+1$ and as it moves its location is tracked by increasing p from 1 to 2. Once the interface reaches very near to grid point $r+1$ and p nearly equals 2, the interface is moved between the grid points $r+1$ and $r+2$. The fraction p, used to track the location of the interface between grid points, is reset to its original value i.e., $p = 1$. This procedure is repeated as the interface moves through the

entire solution domain. Basically the method uses the Stefan condition (Eq. 3.16) to track the solidification front in each time step [8].

To calculate the amount of solid formed in one time step, the partial derivatives in the Stefan condition (Eq. 3.22) are approximated using a three point Lagrange interpolation formula [8] given by:

$$f(x) = \frac{(x-a_1)(x-a_2)}{(a_0-a_1)(a_0-a_2)}f(a_0) + \frac{(x-a_0)(x-a_2)}{(a_1-a_0)(a_1-a_2)}f(a_1) + \frac{(x-a_0)(x-a_1)}{(a_2-a_0)(a_2-a_1)}f(a_2) \tag{4.18}$$

where a_0, a_1, a_2 are any three successive grid points. Differentiating Eq. 4.18 with respect to x we get

$$\frac{df}{dx} = \frac{(x-a_1)+(x-a_2)}{(a_0-a_1)(a_0-a_2)}f(a_0) + \frac{(x-a_0)+(x-a_2)}{(a_1-a_0)(a_1-a_2)}f(a_1) + \frac{(x-a_0)+(x-a_1)}{(a_2-a_0)(a_2-a_1)}f(a_2) \tag{4.19}$$

Equation 4.19 is used as approximations for the partial derivative terms in Eq. 3.25, which is given as:

$$-\frac{k_s}{k_o}\left(\frac{\partial\theta}{\partial\zeta}\right)_s + \frac{k_l}{k_o}\left(\frac{\partial\theta}{\partial\zeta}\right)_l = -\frac{HL^2}{c_{po}Li^2_{ref}(T_p-T_a)}\frac{\partial\delta}{\partial\tau} \qquad at \quad \zeta=\delta, \qquad \tau>0$$

In the solid alumina layer, the points a_0, a_1 and a_2 represents the grid points $(r-2)\Delta\zeta, (r-1)\Delta\zeta$ and $(r-1+p)\Delta\zeta$, respectively, in Fig. 4.5 and the corresponding $f(a_0), f(a_1)$ and $f(a_2)$ represent the dimensionless temperatures $\theta_{r-2}, \theta_{r-1}$ and θ_i, respectively, in the solid layer. Using these grid points, the first term on the left hand side of Eq. 3.25 can be approximated as:

$$\left(\frac{\partial\theta}{\partial\zeta}\right)_s = \frac{p}{(p+1)\Delta\zeta}\theta_{r-2} - \frac{(p+1)}{p\Delta\zeta}\theta_{r-1} + \frac{(2p+1)}{p(p+1)\Delta\zeta}\theta_i \tag{4.20}$$

where θ_i is the fusion temperature of alumina.

Similarly in the liquid layer the points a_0, a_1 and a_2 represents the grid points $(r-1+p)\Delta\zeta, (r+2)\Delta\zeta$ and $(r+3)\Delta\zeta$, respectively, in Fig. 4.5 and the corresponding $f(a_0), f(a_1)$ and $f(a_2)$ represent the dimensionless temperatures θ_i, θ_{r+2} and θ_{r+3}, respectively. Using these grid points, the second term on the left hand side in Eq. 3.25 can be approximated as

$$\left(\frac{\partial\theta}{\partial\zeta}\right)_l = \frac{(2p-7)}{(p-3)(p-4)\Delta\zeta}\theta_i + \frac{(p-4)}{(p-3)\Delta\zeta}\theta_{r+2} + \frac{(p-3)}{(4-p)\Delta\zeta}\theta_{r+3} \tag{4.21}$$

The derivative on the right hand side of Eq. 3.25 can be approximated as

$$\frac{\partial\delta}{\partial\tau} = \frac{p^+ - p}{\Delta\tau}\Delta\zeta \tag{4.22}$$

where

$p \equiv$ location of the solid/liquid interface at time τ

$p^+ \equiv$ location of the solid/liquid interface at time $\tau + \Delta\tau$

Finally combining Eqs. 4.20, 4.21 and 4.22 yields

$$\frac{\Delta\tau}{\Delta\zeta D}\frac{k_s}{k_o}\left(\frac{p}{(p+1)\Delta\zeta}\theta_{r-2} - \frac{(p+1)}{p\Delta\zeta}\theta_{r-1} + \frac{(2p+1)}{p(p+1)\Delta\zeta}\theta_i\right) -$$

$$\frac{\Delta\tau}{\Delta\zeta D}\frac{k_l}{k_o}\left(\frac{(2p-7)}{(p-3)(p-4)\Delta\zeta}\theta_i + \frac{(p-4)}{(p-3)\Delta\zeta}\theta_{r+2} + \frac{(p-3)}{(4-p)\Delta\zeta}\theta_{r+3}\right) = p^+ - p \tag{4.23}$$

where

$$D = \frac{HL^2}{c_{po}Li^2_{ref}(T_p - T_a)}$$

$k_l \equiv$ average thermal conductivity of alumina over the three points a_0, a_1 and a_2 in the liquid region

$k_s \equiv$ average thermal conductivity of alumina over the three points a_0, a_1 and a_2 in the solid region

Equation 4.23 is solved for p^+ in each time step, which basically gives the distance the solid/liquid interface moves in one time step. In Fig. 4.5 the values of i_- and i_+ are calculated using the location of the solidification interface found from Eq. 4.23.

$$i_- = (p^+ - 1)\Delta\zeta \tag{4.24}$$

$$i_+ = (2 - p^+)\Delta\zeta \tag{4.25}$$

Because the temperature at the interface is known and because it is also assumed that solidification occurs at a single finite temperature, the solidification interface can be considered as a constant temperature boundary condition for the control volumes on either side of the interface. The size of these control volumes on either side of the interface is calculated using Eqs. 4.24 and 4.25.

In Fig. 4.5 the grid points r and $r+1$ represent the control volumes surrounding the solidification interface at which the constant temperature boundary condition is applied. Becuase the solidification interface is referenced to grid points r and $r+1$, their locations remain fixed rather than moving with the center of the control volumes.

Control Volume r

For control volume r the solidification interface is at a distance i_- from the grid point r on the right side as shown in Fig. 4.5. Hence the volume of this one-dimensional control volume is $((\Delta\zeta/2) + i_-)$ x 1 x 1. Integrating Eq. 3.21 over the control volume represented by grid point r result in:

$$\frac{\rho c_p}{\rho_o c_{po}}(\theta_P - \theta_p^o)\frac{(\Delta\zeta/2) + i_-}{\Delta\tau} = \frac{L i_{ref}^2}{L^2}\left[\frac{k_e}{k_o}\frac{\theta_i - \theta_P}{i_-} - \frac{k_w}{k_o}\frac{\theta_P - \theta_W}{\Delta\zeta}\right] +$$

$$\frac{1}{L}\frac{dL}{d\tau}\left[\frac{\rho c_p}{\rho_o c_{po}}(\zeta\theta)_i - \frac{\rho c_p}{\rho_o c_{po}}\frac{(\zeta\theta)_P + (\zeta\theta)_W}{2} - \frac{\rho c_p}{\rho_o c_{po}}\theta_P(\Delta\zeta/2 + i_-)\right] \tag{4.26}$$

Equation 4.26 can be written in a more generalized and useful form [13] as

$$a_P\theta_P = a_E\theta_E + a_W\theta_W + b \tag{4.27}$$

where

$$a_E = 0 \tag{4.28a}$$

$$a_W = \frac{Li_{ref}^2}{L^2}\frac{k_w}{k_o\Delta\zeta} - \frac{1}{L}\frac{dL}{d\tau}\frac{\rho c_p}{\rho_o c_{po}}\frac{\zeta_W}{2} \tag{4.28b}$$

$$a_P^o = \frac{\rho c_p}{\rho_o c_{po}}\frac{(\Delta\zeta/2) + i_-}{\Delta\tau} \tag{4.28c}$$

$$b = a_P^o\theta_P^o + S_u \tag{4.28d}$$

$$a_P = \frac{Li_{ref}^2}{L^2}\frac{k_w}{k_o\Delta\zeta} + \frac{1}{L}\frac{dL}{d\tau}\frac{\rho c_p}{\rho_o c_{po}}\frac{\zeta_P}{2} + \frac{1}{L}\frac{dL}{d\tau}\frac{\rho c_p}{\rho_o c_{po}}(\Delta\zeta/2 + i_-) + a_P^o - S_P \tag{4.28e}$$

$$S_P = -\frac{k_e}{k_o}\frac{1}{i_+} \tag{4.28f}$$

$$S_u = \frac{Li_{ref}^2}{L^2}\frac{k_w}{k_o}\frac{\theta_i}{i_+} + \frac{1}{L}\frac{dL}{d\tau}\frac{\rho c_p}{\rho_o c_{po}}(\zeta\theta)_i \tag{4.28g}$$

The values of S_u and S_P are assigned based on the source term model $S = S_u + S_P\theta_P$ [13].

Control Volume $r+1$

Similarly for the control volume $r+1$, the solidification interface is at a distance i_+ from the grid point $r+1$ on the left side as shown in Fig. 4.5. Hence the volume of this one-dimensional control volume is $((\Delta\zeta/2)+i_+)$ x 1 x 1. Integrating Eq. 3.21 over the control volume represented by the grid point $r+1$ yields:

$$\frac{\rho c_p}{\rho_o c_{po}}(\theta_P-\theta_P^o)\frac{(\Delta\zeta/2)+i_+}{\Delta\tau}=\frac{Li_{ref}^2}{L^2}\left[\frac{k_e}{k_o}\frac{\theta_E-\theta_P}{\Delta\zeta}-\frac{k_w}{k_o}\frac{\theta_P-\theta_i}{i_+}\right]+$$

$$\frac{1}{L}\frac{dL}{d\tau}\left[\frac{\rho c_p}{\rho_o c_{po}}\frac{(\zeta\theta)_E+(\zeta\theta)_P}{2}-\frac{\rho c_p}{\rho_o c_{po}}(\zeta\theta)_i-\frac{\rho c_p}{\rho_o c_{po}}\theta_P(\Delta\zeta/2+i_+)\right] \tag{4.29}$$

Equation 4.29 can be written in a more generalized and useful form [13] as

$$a_P\theta_P=a_E\theta_E+a_W\theta_W+b \tag{4.30}$$

where

$$a_E=\frac{Li_{ref}^2}{L^2}\frac{k_e}{k_o\Delta\zeta}+\frac{1}{L}\frac{dL}{d\tau}\frac{\rho c_p}{\rho_o c_{po}}\frac{\zeta_E}{2} \tag{4.31a}$$

$$a_W=0 \tag{4.31b}$$

$$a_P^o=\frac{\rho c_p}{\rho_o c_{po}}\frac{(\Delta\zeta/2)+i_+}{\Delta\tau} \tag{4.31c}$$

$$b=a_P^o\theta_P^o+S_u \tag{4.31d}$$

$$a_P=\frac{Li_{ref}^2}{L^2}\frac{k_e}{k_o\Delta\zeta}-\frac{1}{L}\frac{dL}{d\tau}\frac{\rho c_p}{\rho_o c_{po}}\frac{\zeta_P}{2}+\frac{1}{L}\frac{dL}{d\tau}\frac{\rho c_p}{\rho_o c_{po}}(\Delta\zeta/2+i_+)+a_P^o-S_P \tag{4.31e}$$

$$S_P = -\frac{k_w}{k_o}\frac{1}{i_+} \tag{4.31f}$$

$$S_u = \frac{Li_{ref}^2}{L^2}\frac{k_w}{k_o}\frac{\theta_i}{i_+} - \frac{1}{L}\frac{dL}{d\tau}\frac{\rho c_p}{\rho_o c_{po}}(\zeta\theta)_i \tag{4.31g}$$

The values of S_u and S_P are assigned based on the source term model $S = S_u + S_P\theta_P$ [13].

In this manner the required number of equations for the unknown temperatures are developed. In the next section a suitable method to solve these equations is discussed.

4.4. Solution of the Discretized Algebraic Equations

The discretized equation should be expressed in matrix form to be solved using common matrix methods. Let the grid points in Fig. 4.4 be numbered as 1,2,3,...,N, with points 1 and N denoting the boundary points. The discretized equations can be written in the form [13]

$$a_i\theta_i = b_i\theta_{i+1} + c_i\theta_{i-1} + d_i \tag{4.32}$$

where

i =1,2,3,...,N

$a_i = a_P$ and $\theta_i = \theta_P$

$b_i = a_E$ and $\theta_{i+1} = \theta_E$

$c_i = a_W$ and $\theta_{i-1} = \theta_W$

$d_i = b$

Since for the boundary grid points 1 and N, $a_W = 0$ and $a_E = 0$, respectively, the

discretized equations in the matrix form can be written as

$$[A][\theta] = [D] \tag{4.33}$$

where the coefficient matrix $[A]$ is a tri-diagonal matrix, $[\theta]$ is the non-dimensional temperature distribution vector, and $[D]$ is a constant vector. These, matrices and vectors are defined by:

$$[\mathrm{A}] = \begin{pmatrix} a_1 & -b_1 & 0 & 0 & 0 & \cdots & 0 \\ -c_2 & a_2 & -b_2 & 0 & 0 & \cdots & 0 \\ 0 & -c_3 & a_3 & -b_3 & 0 & \cdots & 0 \\ \vdots & \ddots & \ddots & \ddots & \vdots & \vdots & \vdots \\ 0 & 0 & 0 & -c_{N-2} & a_{N-2} & -b_{N-2} & 0 \\ 0 & 0 & 0 & 0 & -c_{N-1} & a_{N-1} & -b_{N-1} \\ 0 & 0 & 0 & 0 & 0 & -c_N & a_N \end{pmatrix} \tag{4.34}$$

$$[\theta] = \begin{pmatrix} \theta_1 & \theta_2 & \cdots & \theta_N \end{pmatrix}^T \tag{4.35}$$

$$[\mathrm{D}] = \begin{pmatrix} d_1 & d_2 & \cdots & d_N \end{pmatrix}^T \tag{4.36}$$

The discretized equations setup in the matrix form are solved using Tri-Diagonal Matrix Algorithm (TDMA) or the Thomas Algorithm [13]. The TDMA uses the forward elimination and backward substitution technique to arrive at the solution. The advantages of using the TDMA method is that it requires less computer storage and computer time compared to other matrix methods.

4.5. Thermal Energy of the Particles

Thermal energy of the particles is assumed to be released as soon as the particles enter the melt layer. Since the thermal energy is released inside the melt layer, the energy is directly added to the layer instead of applying it through the boundary condition. The volume of the particles deposited in each time step is very small compared to the size of the control volume. Hence the deposited alumina particles are assumed to affect only the control volume EE, at the boundary, as shown in Fig. 4.4. To account for the thermal energy of the deposited alumina particles, a volume-averaged temperature is calculated, and assigned to the grid point of the top control volume EE. In each time step before applying the constant heat flux boundary condition to the control volume EE, the alumina particle are deposited and the thermal energy gained by the control volume EE is equated to the energy bought in by the deposited particles over one time step. This is accomplished by performing an energy balance on the control volume EE near the boundary, which yields:

$$E_{released} = E_{gained} \tag{4.37}$$

where

$E_{released} \equiv$ energy released by the particles in one time step

$E_{gained} \equiv$ energy gained by the control volume near the top surface from the particles in one time step

Equating the energy released by the particles and the energy gained by the control volume we get,

$$m_{pp}c_p(T_p - T_{avg}) = m_{cv}c_p(T_{avg} - T_N) \tag{4.38}$$

where

$c_p \equiv$ specific heat capacity of alumina

$m_{pp} \equiv$ mass of the particles deposited in one time step

$m_{cv} \equiv$ mass of the alumina in the top surface control volume EE

$T_p \equiv$ temperature of the incoming particles

$T_N \equiv$ temperature of the control volume near the top surface

$T_{avg} \equiv$ temperature of the control volume after the deposition of the particles

The average temperature of the control volume at the surface after the addition of the particles is given by

$$T_{avg} = \frac{m_{pp}}{m_{pp} + m_{cv}} T_p + \frac{m_{cv}}{m_{pp} + m_{cv}} T_N \tag{4.39}$$

4.6. Thermo-physical Properties of Alumina

A function is developed to account for the temperature dependence of the thermo-physical properties; namely thermal conductivity and specific heat capacity. A power law is used to fit a curve to the temperature dependent property data provided by the material properties package reference manual [17]. There is a 65% change in the thermal conductivity over the operating temperature range of 1600 K to 5000 K which shows the importance of accounting for the variability in the thermo-physical properties with temperature. The specific heat capacity of the solid alumina varies by 10% over the temperature range of 1500 K to 2327 K. The density of alumina was found to be a constant at $4000 kg/m^3$ in both liquid and solid phase of alumina [17].

Equation 4.40 represents the form of the power law to which the thermal conductivity and specific heat capacity data are fit,

$$\phi = aT^b \tag{4.40}$$

where

$\phi \equiv$ either k or c_p

$a, b \equiv$ constants from the data fit

Figure 4.6 shows the variation in thermal conductivity of alumina with temperature. Figure 4.7 shows the variation in the specific heat capacity of solid alumina with temperature over the range 1000 K to 2327 K. The specific heat capacity remains a constant at approximately 1420 J/kgK throughout the liquid alumina region [17].

Figure 4.8 shows the effect of the temperature dependence of the thermo-physical properties of alumina on the temperature distribution of the alumina layer. A maximum increase of about 13% in the temperature in the alumina layer surface is observed when the temperature dependence of the thermo-physical properties of alumina are taken into account.

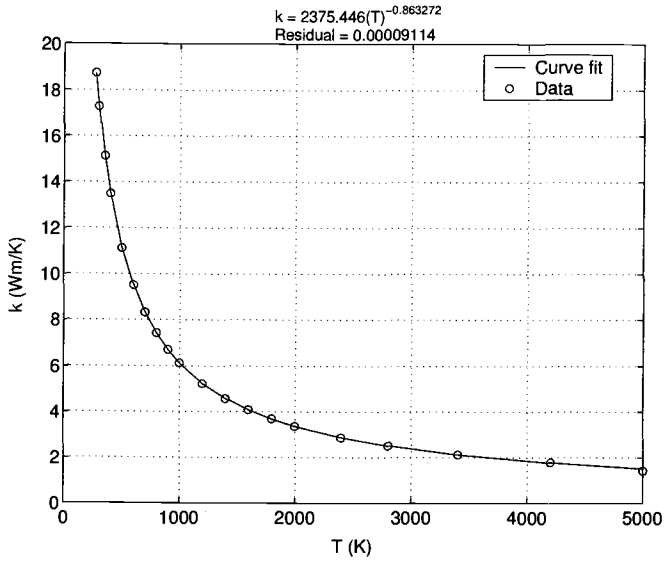

Figure 4.6. Variation in thermal conductivity of alumina with temperature.

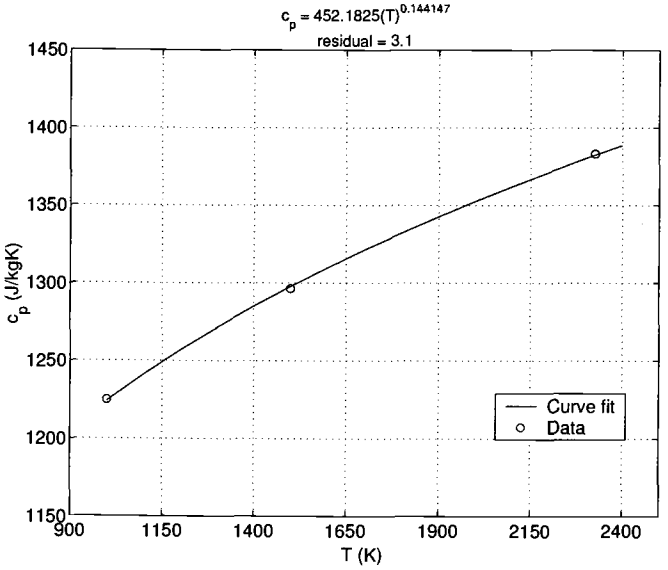

Figure 4.7. Variation in specific heat capacity of solid alumina with temperature.

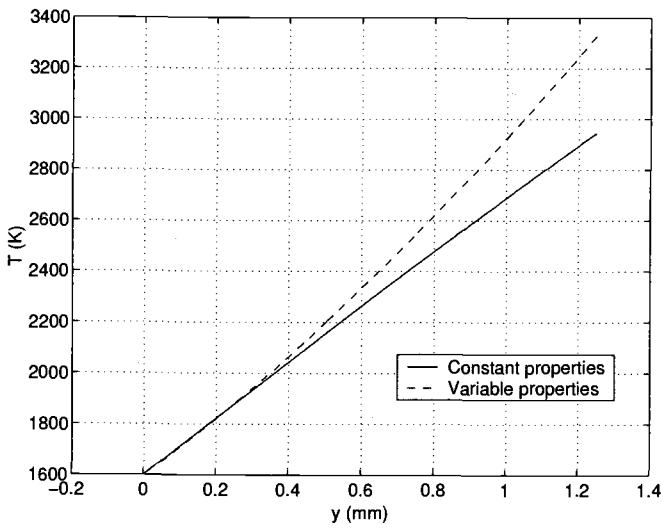

Figure 4.8. Effect of the temperature dependence of the thermo-physical properties of alumina on the temperature distribution for $\dot{m}''_p = 1kg/m^2s$ and $T_p = 2800$ K and $q''_{gas} = 3MW/m^2$ at time $t = 5s$.

4.7. Computational Scheme

The computational scheme involves three loops, one outer loop to step forward in time and two inner loops, consisting of one inner loop for discretizing the equations and the second inner loop for solving the discretized equations using the TDMA solver. All the properties in the equations are calculated using the temperature from the previous time step. This way the non-linearity from the temperature dependent properties are eliminated and results in a set of linear discretized equations. A relatively small time step is used in order to get an acceptable convergent solution at the end of each time step. Also, the change in the temperature distribution between two consecutive time steps is so small that the properties evaluated from the previous time step are a good representation of the properties in the current time step. Equations 4.7 to 4.30 are used to set up a system of linear algebraic equations in the form given by Eq. 4.33 that can be solved using the TDMA method. Meanwhile, the moving boundary due to solidification of alumina is tracked with time. The procedure is also illustrated using the flowchart shown in Fig 4.7.

The computational procedure can be summarized as follows:

1. Read the material properties of alumina at the reference temperature.

2. Read the gas heat flux, particle mass flux and particle velocity.

3. Calculate the particle kinetic energy and add it to the gas heat flux.

4. Calculate the initial reference length and time reference.

5. Calculate the spatial step and time step.

6. Set up the grid for the initial thin alumina layer.

7. Assign initial and boundary conditions.

8. Calculate the mass of the new particles deposited.

9. Calculate the new reference length.

10. Volume average the temperature of the top surface node based on the deposited mass.

11. Calculate the thermo-physical properties.

12. If the temperature of the surface exposed to the mass flux is greater than melting temperature of alumina, find the location of the solid/liquid alumina interface.

13. Find the coefficients a_w, a_e, a_p, b for all internal grid points.

14. Find the coefficients a_w, a_e, a_p, b for the grid point 1 by applying the constant temperature boundary condition.

15. If the temperature of the surface exposed to the mass flux is less than the melting temperature of alumina, add the latent heat of solidification to the surface heat flux.

16. Find the coefficients a_w, a_e, a_p, b for the grid point N by applying the constant heat flux boundary condition.

17. If the temperature of the surface exposed to the mass flux is greater than the melting temperature of alumina, find the coefficients a_w, a_e, a_p, b for the grid points r and $r+1$ near the solid/liquid alumina interface.

18. Set up the coefficient matrix A and D

19. Solve this system of algebraic equations using TDMA to get the new temperature distribution.

20. Store the results.

21. March to the next time step.

22. Repeat the steps 7-20 until the required time is reached.

4.8. Development of the Computer Code

Based on the above procedure a computer code was developed which performs the following calculations:

1. Find the temperature distribution in the alumina layer.

2. Find and track the growth of the solidification of the solid alumina layer.

3. Investigate the effect of the temperature dependence of the thermo-physical properties of alumina on the heat transfer characteristics.

4. Investigate the effect of the variation in the mass flux of the alumina particles on the growth of the solid layer and its effect on the heat transferred to the ablative surface.

5. Investigate the effect of variations in gas heat flux on the growth of the solid layer and its effect on on heat transferred to the ablative surface.

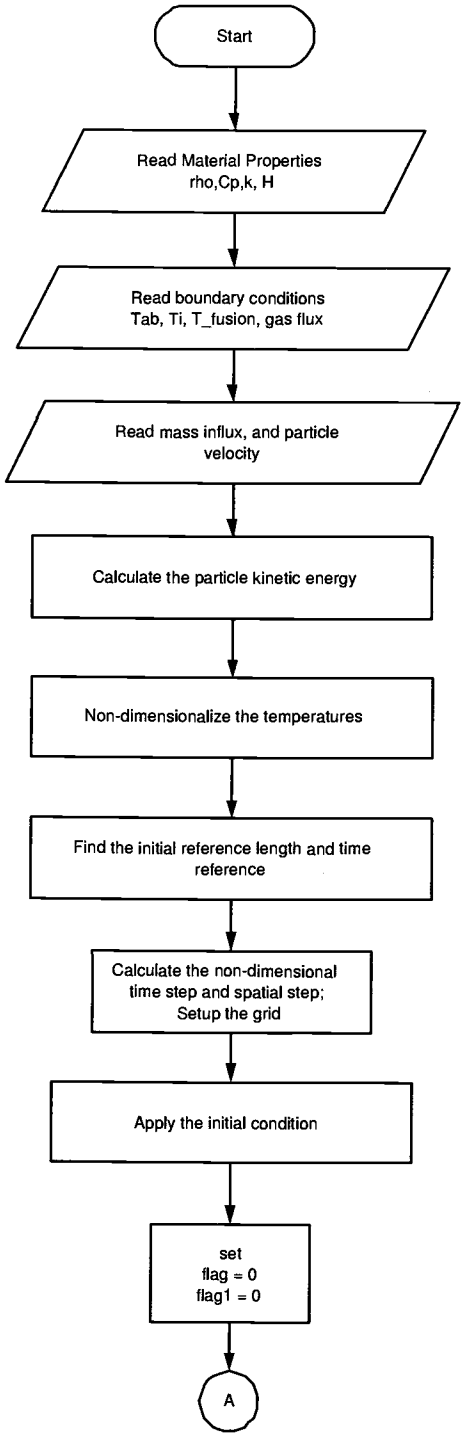

Figure 4.9. Flow chart

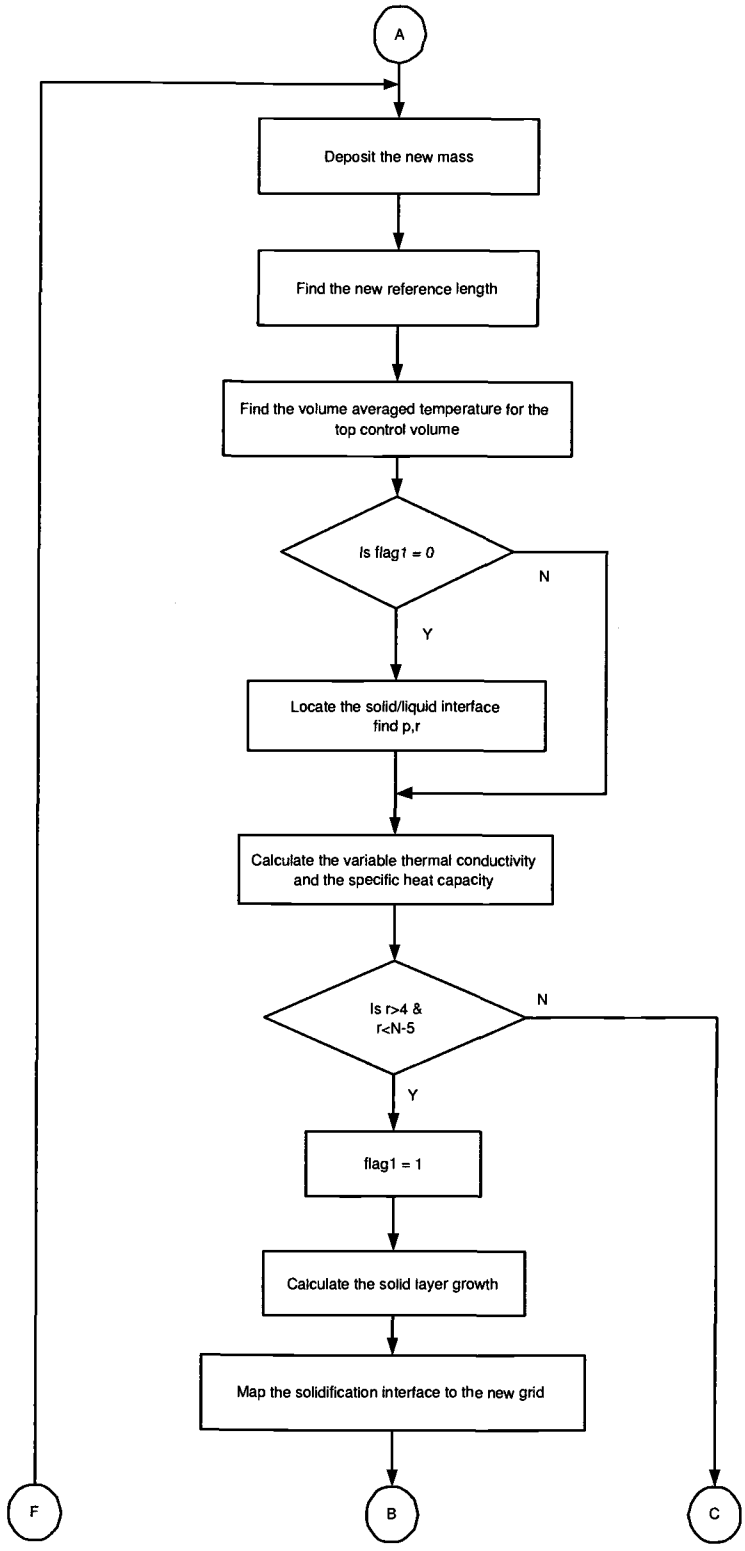

Figure 4.9. Flow chart (continued)

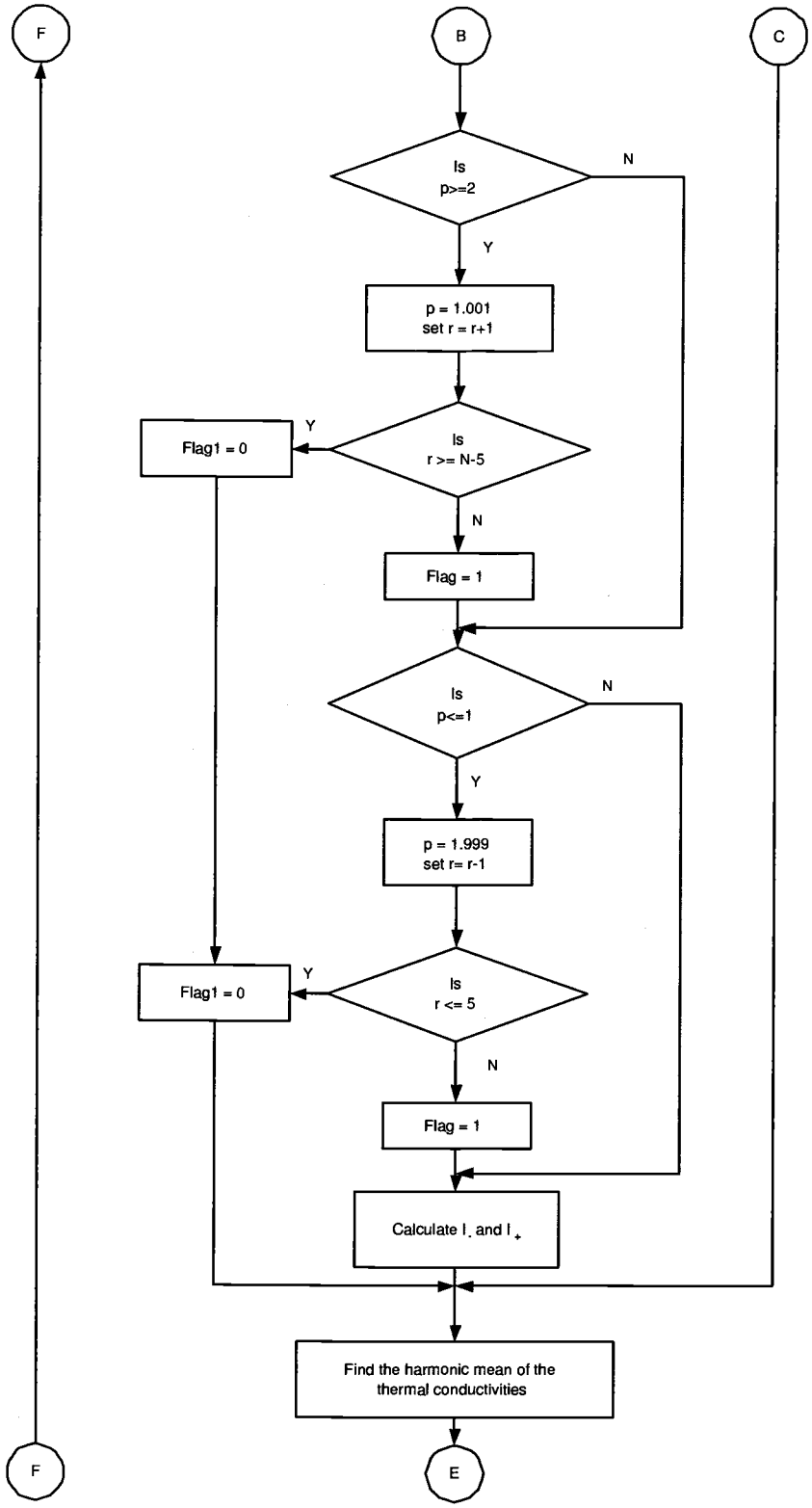

Figure 4.9. Flow chart (continued)

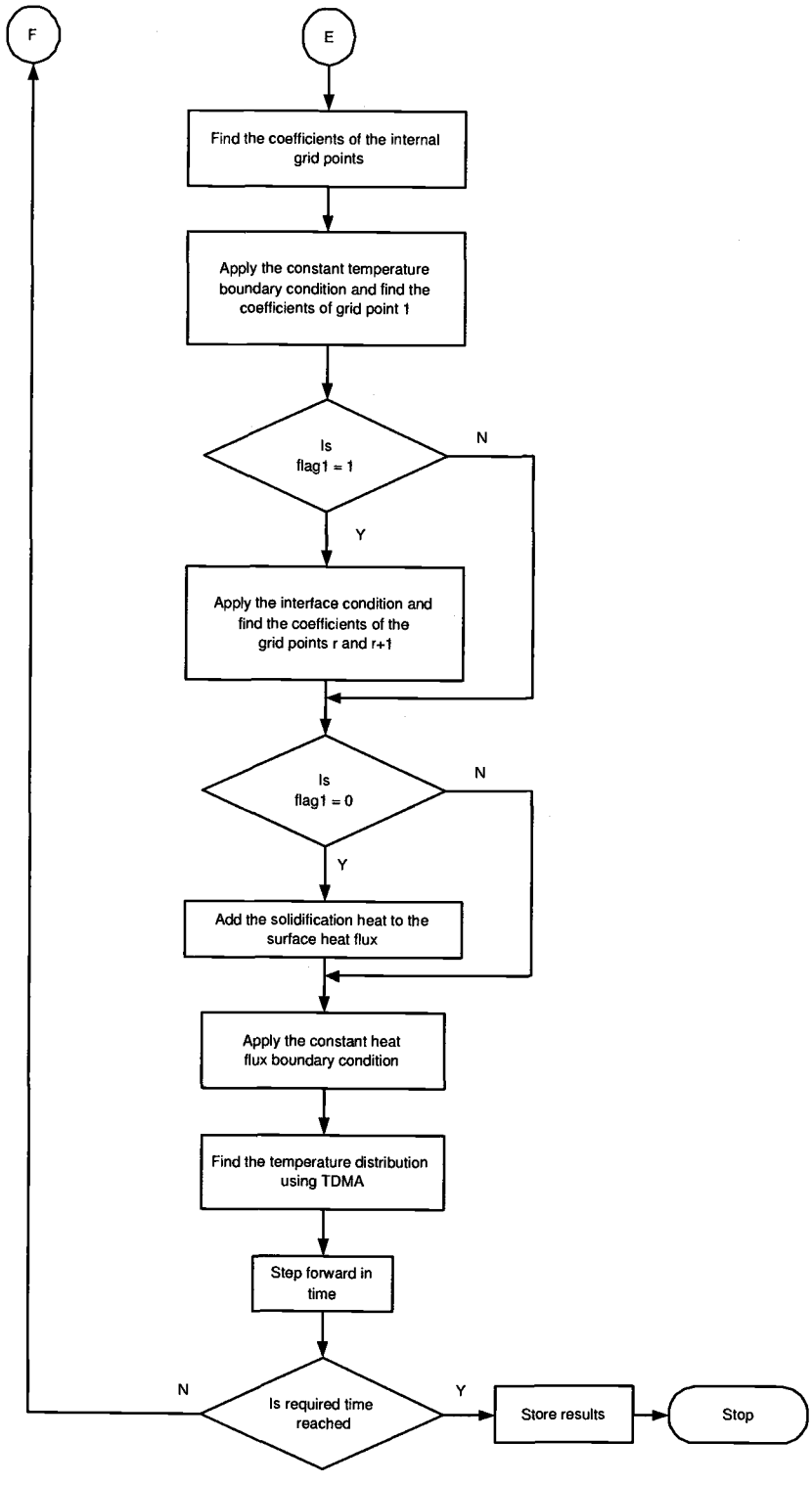

Figure 4.9. Flow chart (continued)

6. Investigate the effect of variations in particle temperature on the growth of the solid layer and its effect on the heat transferred to the ablative surface.

4.9. Limitations of the Computational Model

The computational model developed in this work was identified to have some drawbacks :

- A low diffusion number should be used inspite of using a fully implicit method so that the solidification interface does not move rapidly from one control volume to the next control volume in a single time step.
- The interface condition can be applied only if there are at least 3 control volumes on either side of the phase change interface because the Lagrangian interpolation method used for tracking the interface is a three point method.

5. MODEL VERIFICATION

Model verification is the process of determining whether the computational model accurately represents the physical and mathematical description of the model and provides an accurate solution to the model [16]. It is accomplished by identifying and quantifying the error in the computational model and solution. There are four common source of error in time-dependent computational simulations:

1. insufficient spatial discretization convergence,
2. insufficient temporal discretization convergence,
3. lack of iterative convergence, and
4. computer programming error

In this section the spatial and temporal convergence for the computational model is discussed under the assumption that the computer code developed is free of errors. Also the model is partially verified using an analytical Stefan solution.

5.1. Spatial and Temporal Convergence

The important step in the verification of a computational model is systematically refining the spatial grid size and the time step. The aim is to estimate the discretization error of the numerical solution. As the grid size and time step approach zero, the discretization error should also approach zero, taking into account the computer round-off error. To check the convergence of this computational model the temperature was taken as the dependent variable and observed during refinement.

Spatial Convergence

To check for spatial convergence the grid should be refined until there is little change in the dependent variable, namely the temperature distribution. The grid refinement for the computational model was done by increasing the number of control volumes or cells in the solution domain. A base case was studied at time $t = 5s$ for a particle mass flux of $1kg/m^2s$, a particle temperature $T_p = 2800$ K and a gas heat flux $q''_{gas} = 3MW/m^2$. The variation in temperature distribution for 100, 200 and 500 control volumes was analyzed and was found that the change in temperature when the grid is refined from 100 cells to 200 cells to be approximately 3 K over a temperature difference of 1727 K. Further refining the grid to 500 cells reduces the error to 1.7 K. This amount of error is taken to be a reasonably low error for this application.

Temporal Convergence

To check for the temporal convergence the grid resolution was fixed and the diffusion number was reduced until there was little change in the temperature distribution. A base case having a mass flux of $1kg/m^2s$, a particle temperature of 2800 K and a gas heat flux of $3MW/m^2$ is analyzed. The temperature distribution for diffusion numbers 0.5, 0.1 and 0.01 for 500 cells was studied and the change in temperature when the diffusion number is decreased from 0.5 to 0.1 was found to be about 0.04 K over a temperature difference of 1727 K. Further decreasing the diffusion number to 0.01 results in a temperature change of about 0.01 K. Based on these observations a diffusion number of 0.01 was used to further study the behavior of the system. Although the number of cells was fixed throughout the calculation

procedure for any given mass flux, it was increased linearly with the mass flux to maintain the same accuracy of the computational solution. Thus spatial and temporal convergence of the numerical solution was ensured.

5.2. Comparison with Stefan Analytical Solution

Comparing a computational solution to an analytical solution is the most accurate and reliable way to quantitatively measure the error in the computational solution. The model built in this work does not have an analytical solution. The best way to assess this computational model is to suitably modify it to closely represent an analytical solution. The closest analytical solution available for this model is the Stefan problem [1]. The Stefan problem is one with a moving boundary, but without an expanding solution domain. Therefore to allow the computational model to closely resemble the Stefan problem, the mass influx was reduced to an insignificantly small value such that the solution domain does not noticeably expand between time steps. The initial condition for the computational model is such that there is sufficient amount of deposited material to establish the grid. The surface heat flux is also reduced to a very low value such that the heat flux does not affect the temperature distribution of alumina layer.

To compare the solution of the computational model with the Stefan analytical solution an initial alumina layer thickness of 10 mm with an uniform temperature of 2800 K was used. A low mass flux of $1mg/m^2s$ was maintained. Figure 5.1 presents the comparison between the computational model solution and the analytical Stefan solution at time $1s, 3s$ and $5s$. The plot shows that the difference in the temperature between the numerical and the analytical solution is about 0.24 K

over a temperature difference of 1200 K. Also in the plot a change in the slope of the curve is identified at the solid/liquid alumina interface. The slope of the curve in the solid region is steeper compared to the liquid alumina region due to heat released from the solidification of alumina. This comparison helps to partially verify the computational model.

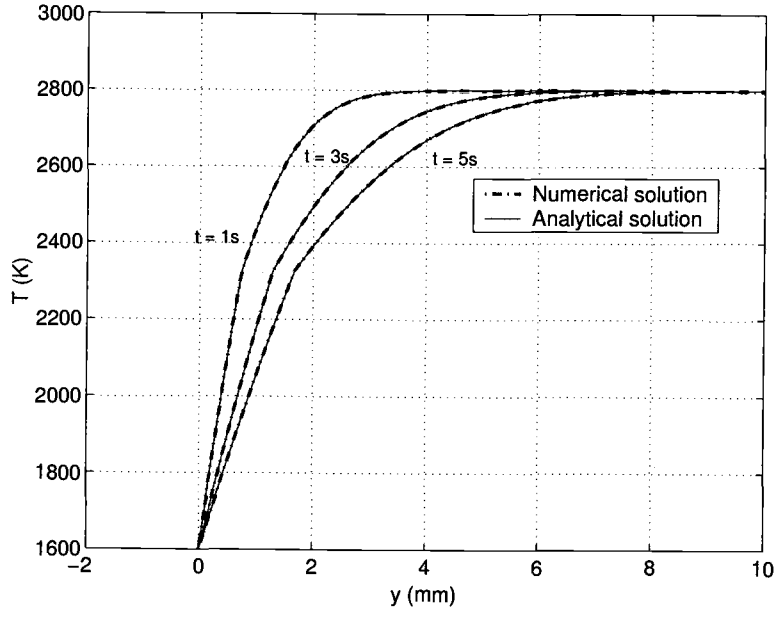

Figure 5.1. Comparison of the predicted numerical solution to the analytical Stefan problem solution.

6. RESULTS AND DISCUSSION

This chapter presents results of the study on solidification dynamics of alumina. A total of 50 cases were used to analyze effects of several parameters on the process. Table 6.1 gives the range of the system variables that were used.

Table 6.1. Test range for the system variables

Variables	*Test Range*
Particle mass flux, $\dot{m}''_p$	$1, 2, 3, 4, 5 kg/m^2 s$
Gas heat flux, q''_{gas}	$1, 3, 5, 7, 9, 11 MW/m^2$
Particle temperature, T_p	2400, 2600, 2800, 3000, 3200 K

The effect of the mass flux, $\dot{m}''_p$, was studied for one base case condition defined as having a particle temperature $T_p = 2800$ K and a gas heat flux $q''_{gas} = 3MW/m^2$. The effect of the particle temperature T_p is presented for the base case gas heat flux $q''_{gas} = 3MW/m^2$ at time $t = 5s$. Similarly the effect of the gas heat flux q''_{gas} is presented for the base case particle temperature $T_p = 2800$ K at time $t = 5s$.

All the particles are assumed to have a uniform velocity of 1650 m/s and the kinetic energy is calculated based on this velocity. The fail temperature of the ablative layer (1600 K), T_a, is used as the reference temperature for the study and the reference thermo-physical properties are evaluated at this temperature. An initial time step, Δt, of $1ms$ was used to form the initial alumina layer for establishing the

grid. But the effect of this initial time step on the system reponse was not investigated. Since the reference length, $L(t)$, is time dependent, using the time dependent length reference for calculating the time reference, $t_{ref} = L(t)^2/\alpha_o$ will make the problem indeterminate. Consequently, the time reference is made independent of the time dependent length reference by using an initial length reference, Li_{ref}, calculated using a fixed time. The time used to calculate the initial length reference was chosen as the total time over which the calculation was to be executed, which is $5s$. Thus the time reference is constant throughout the calculation but the length reference is calculated at every time step.

6.1. Energy distribution

Table 6.2 shows the distribution of energy at time $t = 0s$ for the base case conditions for various mass fluxes. The table basically shows the various sources by which energy is added to the system and percentage contribution of each source to the heat transferred to the ablative surface.

Table 6.2. Energy distribution for base case condition at $t = 0s$.

$\dot{m}_p$, kg/m^2s	1	2	3	4	5
q''_{ab}, MW/m^2	7.01	10.985	14.925	18.785	22.55
q''_{gas}/q''_{ab}	0.428	0.273	0.201	0.159	0.133
q''_{KE}/q''_{ab}	0.194	0.248	0.273	0.29	0.30
$q''_{particle}/q''_{ab}$	0.234	0.298	0.328	0.348	0.36
q''_{gen}/q''_{ab}	0.144	0.181	0.1966	0.201	0.202

6.2. Temperature variations in the alumina

The effect of particle mass flux, $\dot{m}''_p$, on the temperature distribution in the alumina for a particle temperature of 2800 K and a gas heat flux of $3MW/m^2s$ is presented in Figs. 6.1 - 6.3. The variation in the temperature distribution is presented at time intervals of $1s$ up to $5s$. The temperature distribution in the alumina, shown in Fig. 6.1, shows a steady increase in temperature for the low mass flux of

$1kg/m^2s$. Figure 6.2 shows the temperature distribution for a mass flux of $3kg/m^2s$. It can be obesrved from the plot that the temperature distribution tends towards asymptotic behavior. As the mass flux is increased to $5kg/m^2s$ (Fig. 6.3), the surface temperature reaches an asymptotic state at 4105 K for the given conditions for $t > 2s$. Once the asymptotic state is reached the deposited particles are quickly heated up to the 4105 K. The surface, and a sizable amount of the liquid alumina layer are maintained at the asymptotic temperature. In Fig. 6.3 about 24% of the liquid alumina layer is maintained at the asymptotic temperature at time $t = 5s$. This asymtotic behavior is related to the amount of mass deposited in any given period of time. For low mass flux the gas heat flux applied on the surface is sufficiently large to heat the entire deposited mass. But as the mass flux is increased a condition is attained quickly where the amount of heat supplied by the gas heat flux is not sufficient to increase the temperature of the deposited mass beyond the asymptotic temperature.

6.2.1. Effect of particle mass flux on the surface temperature of the alumina

The effect of the particle mass flux, $\dot{m}''_p$, on the surface temperature, T_s, of the alumina at time $t = 5s$ for a particle temperature of $T_p = 2800$ K and gas heat flux of $q''_{gas} = 3MW/m^2$ is presented in Fig. 6.4. For the given particle temperature and gas heat flux, as the mass flux increases the surface temperature shows a steep increase for the low mass fluxes then reaches a maximum surface temperature of 4370 K near a mass flux of $2.5kg/m^2s$. Further increase in the mass

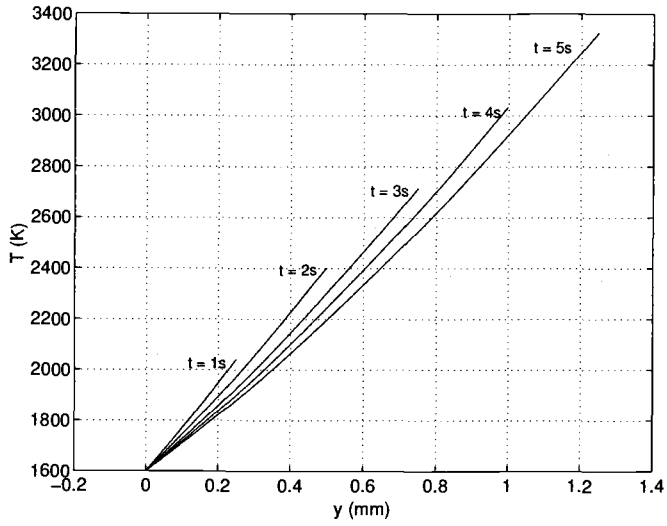

Figure 6.1. Temperature distribution in the alumina in steps of 1s for $\dot{m}''_p = 1kg/m^2s$ having $T_p = 2800$ K and $q''_{gas} = 3MW/m^2$.

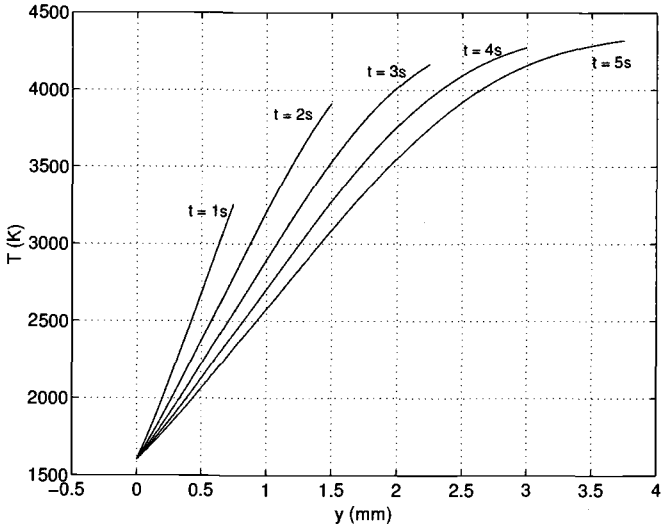

Figure 6.2. Temperature distribution in the alumina in steps of 1s for $\dot{m}''_p = 3kg/m^2s$ having $T_p = 2800$ K and $q''_{gas} = 3MW/m^2$.

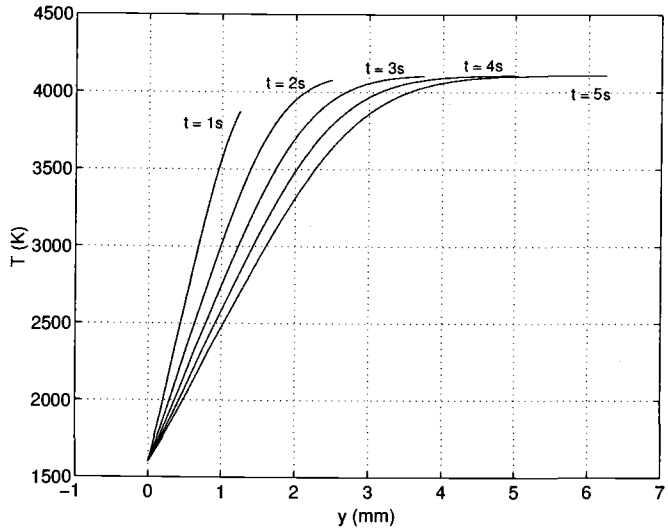

Figure 6.3. Temperature distribution in the alumina in steps of 1s for $\dot{m}''_p = 5kg/m^2s$ having $T_p = 2800$ K and $q''_{gas} = 3MW/m^2$.

flux causes the surface temperature to decrease slowly, reaching a minimum of 4107 K for a mass flux of $5kg/m^2s$ the largest particle mass flux considered in the present investigation. This behavior can be attributed to the increase in the thermal energy storage capacity of the deposited alumina. From Fig. 6.4 it can be observed that the surface temperature of the alumina is higher than the melting temperature of alumina which is 2327 K. So basically the incoming particles absorbs and stores some energy from the surface heat flux and their temperatures rise. But the amount of energy the incoming particles can store depends on the mass flux of the particles. Thus, cases of higher mass flux results in higher energy storage capacity of the alumina and hence the surface temperature of the alumina drops to lower values with the increasing mass flux.

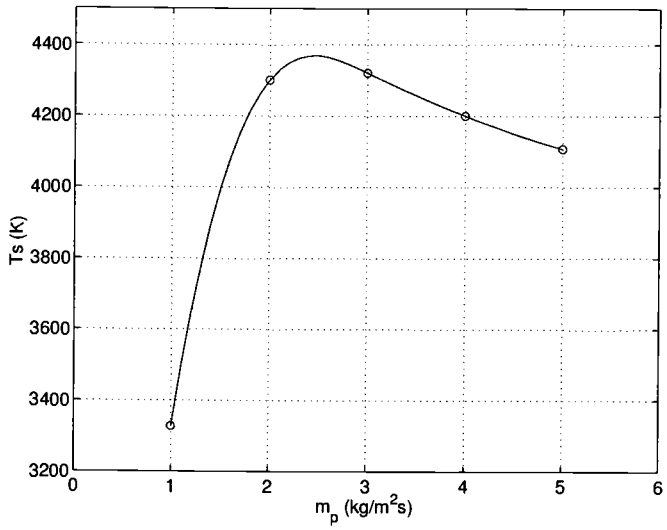

Figure 6.4. Variation of surface temperature with mass flux at time $t = 5s$ for $T_p = 2800K$ and $q''_{gas} = 3MW/m^2$.

6.2.2. Effect of gas heat flux on the surface temperature of the alumina

The variation of surface temperature, T_s, with gas heat flux, q''_{gas}, for a particle temperature of 2800 K is presented in Fig. 6.5. The gas heat flux is varied from $1MW/m^2$ to $11MW/m^2$ and the effect of the gas heat flux is presented for various mass fluxes at time $t = 5s$. A steep increase in the surface temperature with increase in the gas heat flux is observed for lower mass flux values. But the rate of increase in the surface temperature decreases as the mass flux is increased. For a mass flux of $1kg/m^2s$ the change in the surface temperature, when the gas heat flux is varied from $1MW/m^2$ to $11MW/m^2$, is about 140%. But if the mass flux is doubled to

$2kg/m^2s$ the increase in the surface temperature with gas flux is only about 83%. Further increasing the mass flux to $5kg/m^2s$ results in an increase in the surface temperature of only about 32%.

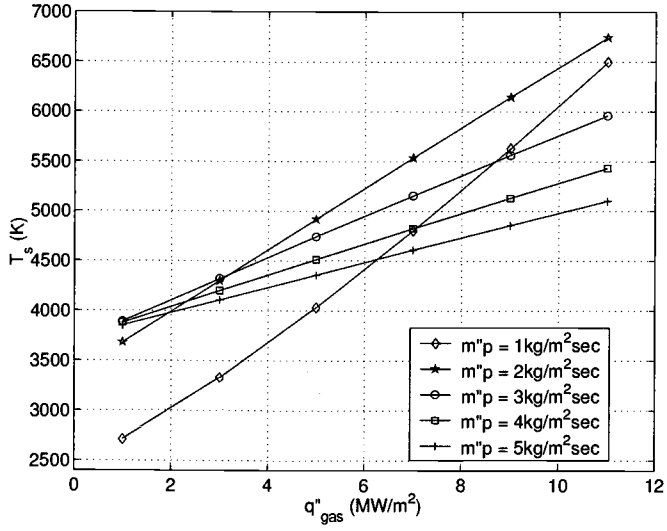

Figure 6.5. Variation of surface temperature with gas heat flux for $T_p = 2800$ K at time $t = 5s$.

6.2.3. Effect of particle temperature on the surface temperature of the alumina

The variation of surface temperature with particle temperature for $q''_{gas} = 3MW/m^2$ is presented in Fig. 6.6. The particle temperature is varied from 2400 K to 3200 K and the effect on the surface temperature is presented for various

mass fluxes at time $t = 5s$. The surface temperature of the alumina increases with increasing particle temperature. The rate of increase of the surface temperature with the particle temperature is the same for mass fluxes that are over $3kg/m^2s$. The range over which the surface temperature varies is different for different mass fluxes. It is interesting to note that the mass fluxes of $2kg/m^2s$ and $3kg/m^2s$ have almost the same range, from 3950 K to 4700 K, over which the surface temperature varies when the particle temperature varies from 2400 K to 3200 K.

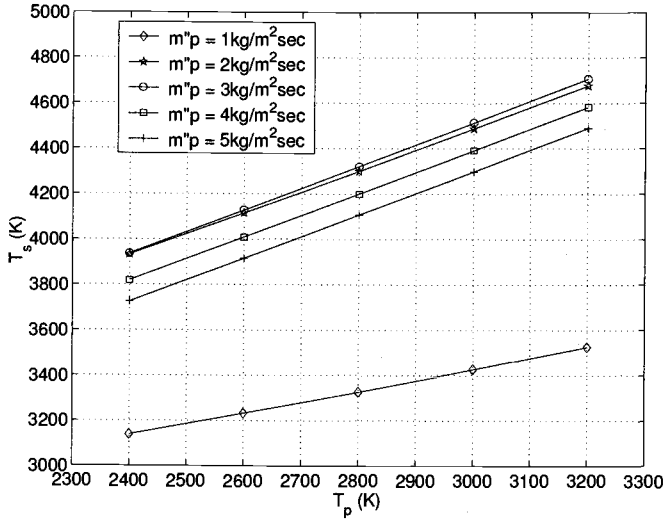

Figure 6.6. Variation of surface temperature with particle temperature for $q''_{gas} = 3MW/m^2$ at time $t = 5s$.

6.3. Solidification growth

Figure. 6.7 shows the growth of the solid alumina layer, δ_s, for different particle mass fluxes. The solidification growth was studied for a particle temperature of 2800 K and a gas heat flux of $3MW/m^2$. The graph shows a linear solidification rate in the early phase of the alumina formation where only the solid alumina layer exists. As the alumina enters a later phase, the liquid alumina layer also begins to grow and the solidification rate decreases. The time taken for the alumina to enter into the later phase decreases with the increase in the particle mass flux. This can be attributed to the larger time scale associated with the solidification rate compared to the deposition rate of alumina particles. It can also be seen from Fig. 6.7 that the growth rate of the solid alumina increases with an increase in the particle mass flux. Figure 6.8 shows the relative solid layer growth rate ($\dot{m}''_s/\dot{m}''_p$) with time. It can be observed from the figure that the solidification rate is much lesser than the particle deposition rate. Also, for the high mass fluxes the ratio ($\dot{m}''_s/\dot{m}''_p$) slowly decreases with time.

Figure 6.9 shows the variation of the relative thickness of the solid alumina layer (δ_s/L) with time. The variation was studied for a particle temperature of 2800 K and a gas heat flux of $3MW/m^2$ for mass flux varying between $1kg/m^2s$ to $5kg/m^2s$. The figure shows that the relative solid layer thickness (δ_s/L) decreases with time approximately exponentially. The rate at which the relative solid thickness (δ_s/L) decreases depends on the particle mass flux $\dot{m}''_p$. The rate of decrease of the relative thickness (δ_s/L) becomes more significant with an increase in the mass flux. Figure. 6.9 shows that the relative solid layer thickness is about 48% at time $t = 5s$ for a mass flux of $1kg/m^2s$ but decreases to 28% when the mass flux is doubled to

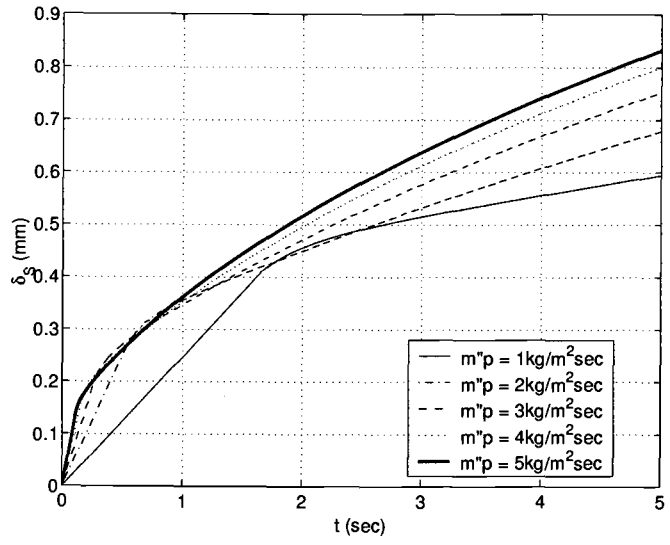

Figure 6.7. Solidification growth for various mass flux for $q''_{gas} = 3MW/m^2$ and $T_p = 2800$ K.

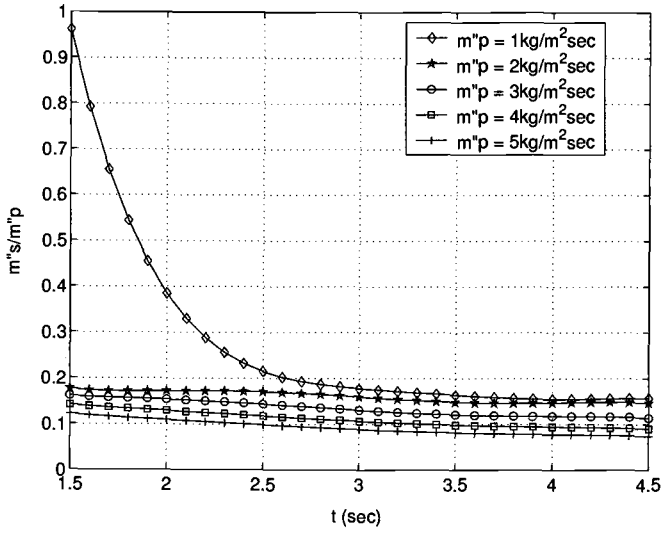

Figure 6.8. Relative solid layer growth rate for various mass flux for $q''_{gas} = 3MW/m^2$ and $T_p = 2800$ K.

$2kg/m^2s$. Further increasing the mass flux to $4kg/m^2s$ decreases the relative solid layer thickness to 16%. This decrease in the relative solid layer thickness can be attributed to the large particle deposition rate and slow solidification growth rate of the solid alumina layer as observed in Fig. 6.8. The change in the relative solid layer thickness with mass flux decreases for higher mass fluxes i.e., there is less than 12% change in the relative thickness when the mass flux increases from $2kg/m^2s$ to $4kg/m^2s$ compared a 20% change when the mass flux is increased from $1kg/m^2s$ to $2kg/m^2s$. So for sufficiently high mass fluxes the relative solid layer thickness becomes asymptotic.

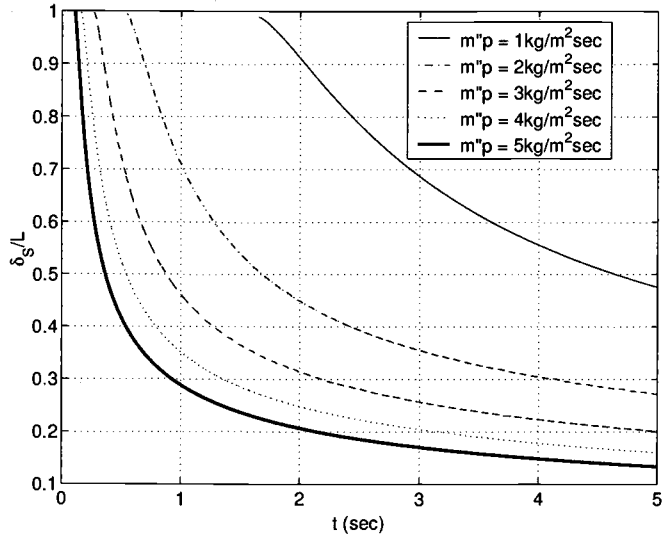

Figure 6.9. Variation in the relative solid layer thickness (δ_s/L) with time for various mass fluxes for $T_p = 2800$K and $q''_{gas} = 3MW/m^2$.

Figure. 6.10 presents the variation in the relative liquid alumina layer thickness (δ_L/L) with time. The variation was studied for a particle temperature of 2800 K and a gas heat flux of $3MW/m^2$ for mass flux varying between $1kg/m^2s$ to $5kg/m^2s$. The graph shows that the relative liquid alumina layer thickness increases with time for all mass fluxes. But the rate at which it increases depends on the mass flux of the particles. The rate also varies with time at which this liquid layer grows. A steep increase in the relative thickness is observed for high mass fluxes. Also the time taken for the liquid alumina layer to grow along with the solid layer decreases with the increase in the mass flux.

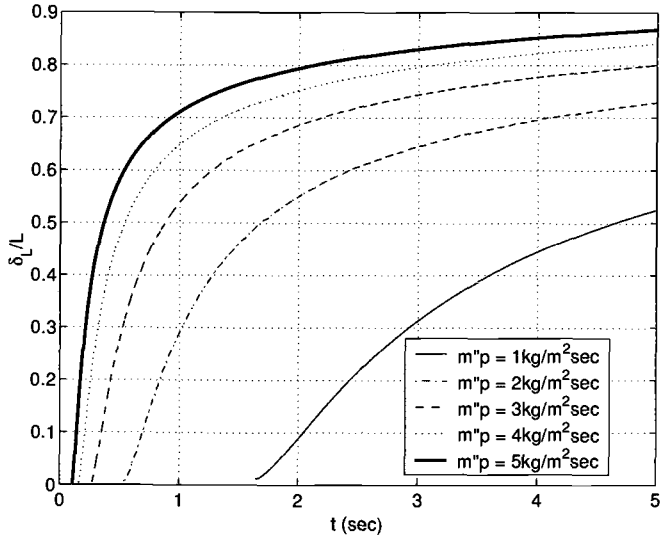

Figure 6.10. Variation in the relative liquid layer thickness (δ_L/L) with time for various mass fluxes for $T_p = 2800$K and $q''_{gas} = 3MW/m^2$.

6.3.1. Effect of gas heat flux on solidification

The effect of gas heat flux on the relative solid layer thickness (δ_s/L) is presented in Fig. 6.11 for a particle temperature $T_p = 2800$ K at time $t = 5s$. The gas heat flux was varied from $1MW/m^2$ to $11MW/m^2$ and the results are studied for particle mass fluxes ranging from $1kg/m^2s$ to $5kg/m^2s$. The effect of the gas heat flux is predominant for the low mass flux of $1kg/m^2s$. For the $1kg/m^2s$ particle mass flux, the relative solid layer thickness decreases from 68% to 22% when the gas heat flux is increased from $1MW/m^2$ to $11MW/m^2$. Increasing the gas heat flux basically increases the heat flux at the solid/liquid alumina interface. This increase in heat flux decreases the solidification rate. The effect of the gas heat flux decreases with the increase in the mass flux. For a mass flux of $5kg/m^2s$ the relative solid layer thickness decreases from 14% to 10% when the gas heat flux is increased from $1MW/m^2$ to $11MW/m^2$. This small difference compared to the low mass flux case can be attributed to a thicker liquid alumina. This thicker layer, due to its increased sensible storage, transfers less heat to the interface and the increase of q''_{gas} has a reduced impact on the solid layer thickness.

Figure 6.12 presents the effects of the gas heat flux q''_{gas} on the relative thickness of the liquid alumina layer (δ_L/L) for a particle temperature of $T_p = 2800$ K at time $t = 5s$. The graph shows that the effect of the gas heat flux on the relative thickness of the liquid alumina layer is predominant for low mass fluxes. The relative thickness increases with increase in gas heat flux. The relative thickness of liquid alumina layer increases from 32% to 78% for a mass flux of $1kg/m^2s$. But for a mass

flux of $5kg/m^2s$ the relative thickness of liquid alumina just increases from 86% to 90%, which is very low compared to the lower mass fluxes.

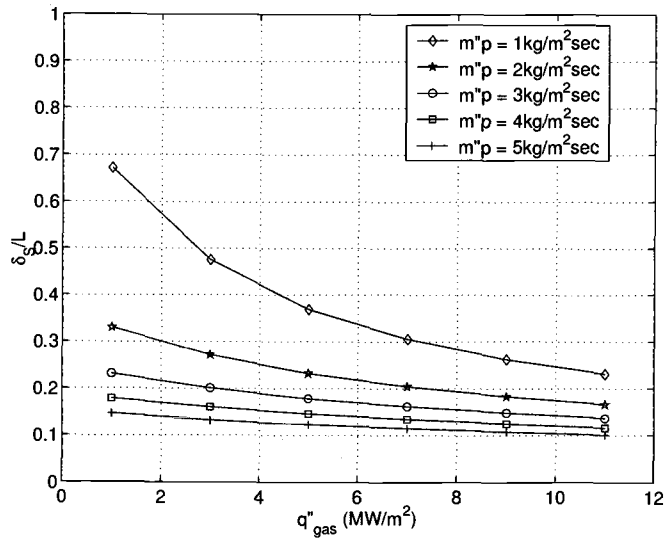

Figure 6.11. Effect of gas heat flux q''_{gas} on the relative solid layer thickness (δ_s/L) for $T_p = 2800$ K at time $t = 5s$.

6.3.2. Effect of particle temperature on solidification

The effect of particle temperature, T_p, on the relative solid layer thickness (δ_S/L) is presented in Fig. 6.13 at time $t = 5s$ for a gas heat flux $q''_{gas} = 3MW/m^2$. The particle temperature is varied from 2400 K to 3200 K and the effect is presented for particle mass fluxes from $1kg/m^2s$ to $5kg/m^2s$. As the particle temperature

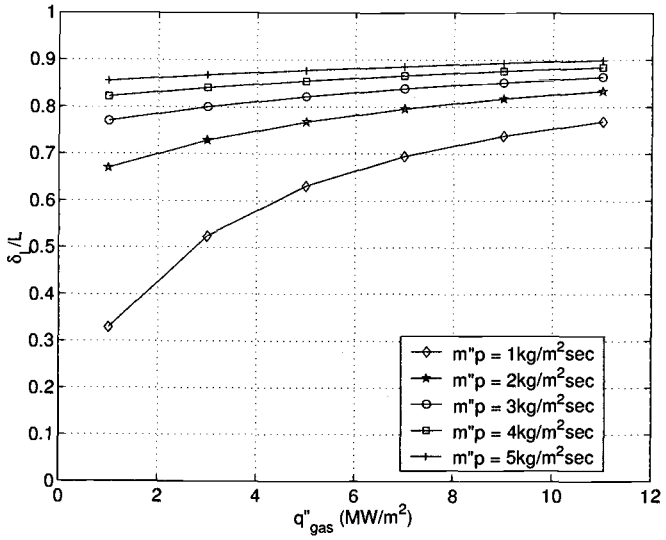

Figure 6.12. Effect of gas heat flux q''_{gas} on the relative liquid layer thickness (δ_L/L) for $T_p = 2800$ K at time $t = 5s$.

is increased the relative solid layer thickness (δ_S/L) decreases. This is because the heat flux to the solid alumina layer increases with particle temperature and causes the solidification rate to decrease. The effect of the particle temperature is approximately linear with the curves having the same slope for all mass fluxes. This linear effect may be attributed to the direct addition of the thermal energy of the particles to the alumina instead of imposing it through a boundary condition.

Figure 6.14 presents the effect of particle temperature, T_p on the relative liquid alumina layer thickness (δ_L/L) for a gas heat flux of $3MW/m^2$ at time $t = 5s$. As the particle temperature increases the relative thickness of the liquid alumina layer also increases. As expected, the increase in the relative thickness of liquid alumina layer is approximately linear with the increase in the particle temperature.

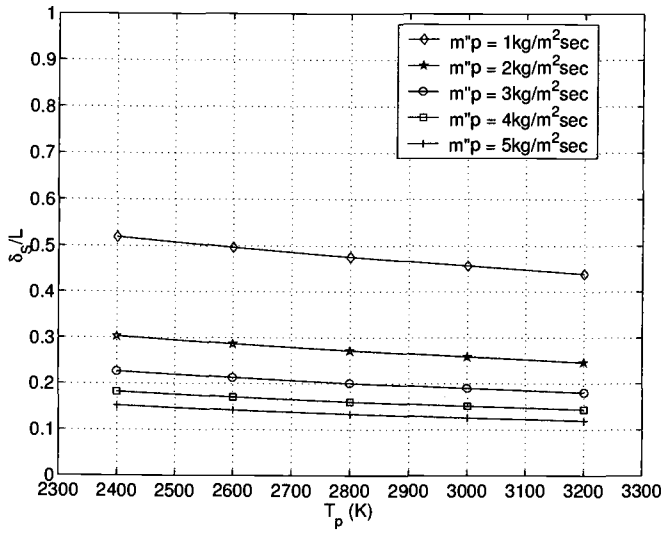

Figure 6.13. Effect of particle temperature T_p on the relative solid layer thickness (δ_S/L) for $q''gas = 3MW/m^2$ at time $t = 5s$.

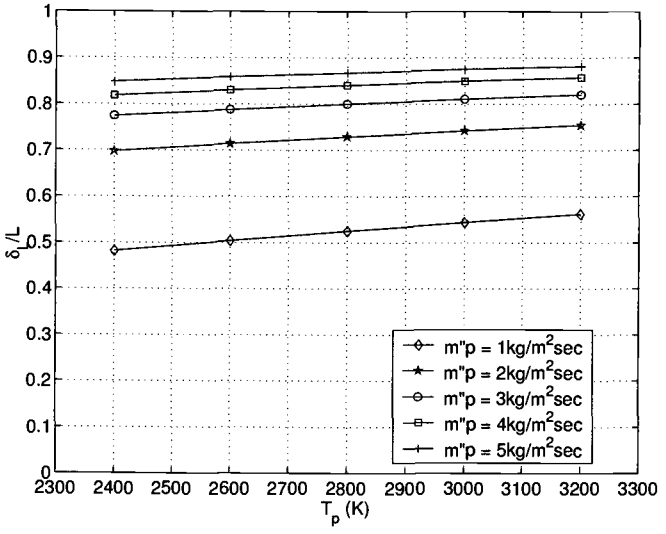

Figure 6.14. Effect of particle temperature T_p on the relative liquid layer thickness (δ_L/L) for $q''gas = 3MW/m^2$ at time $t = 5s$.

6.4. Heat flux at the solid/liquid alumina interface

Figure. 6.15 shows the variation of the heat flux at the solid/liquid alumina interface with time. The effect of the particle mass flux on the interface heat flux is studied for a particle temperature of 2800 K and a gas heat flux of $3MW/m^2$. The heat flux at the solid/liquid alumina interface is the energy coming out of the liquid alumina layer. This does not include the latent heat of solidification of alumina. It can be observed from the graph that the solid/liquid interface heat flux decreases with time. The heat flux at the interface decreases with time due to the development of the liquid alumina layer. The rate of decrease of the heat flux at the interface depends on the particle mass flux. For a high mass flux of $5kg/m^2s$ the interface heat flux decreases approximately exponentially from $13MW/m^2$ to as low as $2.5MW/m^2$, which is about a 81% decrease in the interface heat flux. For a low mass flux of $1kg/m^2s$ the heat flux decreases by 20%. A higher mass flux results in a thicker alumina which basically increases the sensible energy storage capacity of alumina and results in a reduced heat flux at the interface. The heat flux at the solid/liquid interface comes into the picture only after solid and liquid alumina layers begin to co-exist. This is the reason why different starting times are observed for different mass fluxes in Fig. 6.15. It takes a longer time in the case of lower mass fluxes for the solid and liquid alumina layer to co-exist.

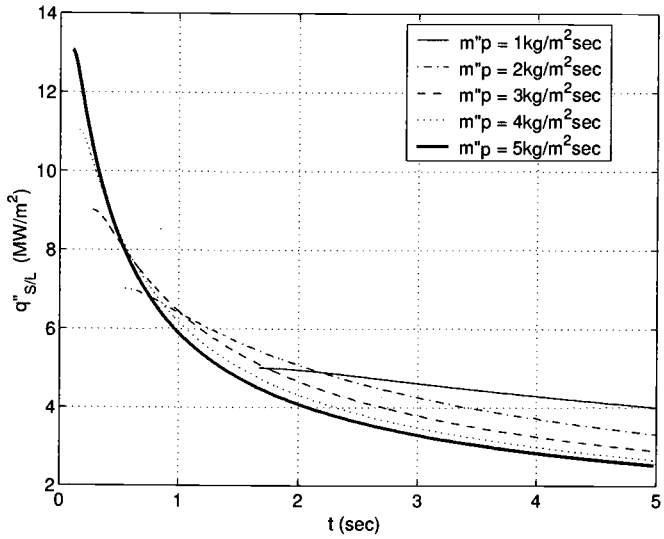

Figure 6.15. Variation of heat flux at the solid/liquid alumina interface for $T_p = 2800$ K and gas heat flux of $q''_{gas} = 3MW/m^2$.

6.4.1. Effect of gas heat flux on the solid/liquid alumina interface heat flux

The effect of the gas heat flux on the solid/liquid alumina interface heat flux is presented in Fig. 6.16 for a particle temperature $T_p = 2800$ K at time $t = 5s$. The gas heat flux is varied from $1MW/m^2$ to $11MW/m^2$ and its effect on the interface heat flux is studied by varying the particle mass flux from $1kg/m^2s$ to $5kg/m^2s$. The interface heat flux increases with the increase in the gas heat flux but the rate of increase depends on the mass flux of the particles. Approximately only 32% of the $11MW/m^2$ gas heat flux is conducted to the solid/liquid interface for a high

mass flux of $5kg/m^2s$ compared to the 77% of the applied gas heat flux for a low mass flux of $1kg/m^2s$.

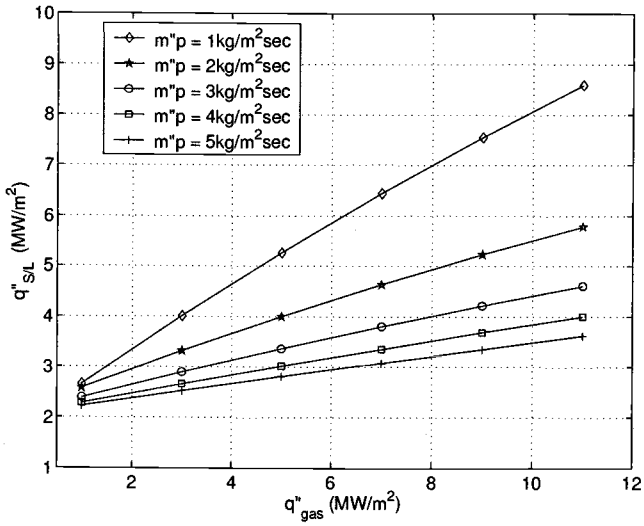

Figure 6.16. Effect of gas heat flux on the solid/liquid alumina interface heat flux for $T_p = 2800$ K at time $t = 5s$.

6.4.2. Effect of particle temperature on the solid/liquid alumina interface heat flux

The effect of the particle temperature on the solid/liquid alumina interface heat flux is presented in Fig. 6.17 for a gas heat flux $q''_{gas} = 3MW/m^2$ at time $t = 5s$. The particle temperature is varied from 2400 K to 3200 K and its effect on the interface heat flux is studied for particle mass flux from $1kg/m^2s$ to $5kg/m^2s$.

Figure 6.17 shows that as the particle temperature increases the interface heat flux also increases. A linear relationship is found to exist between the particle temperature and its effect on the solid/liquid alumina interface heat flux, where the slope is independent of the mass flux.

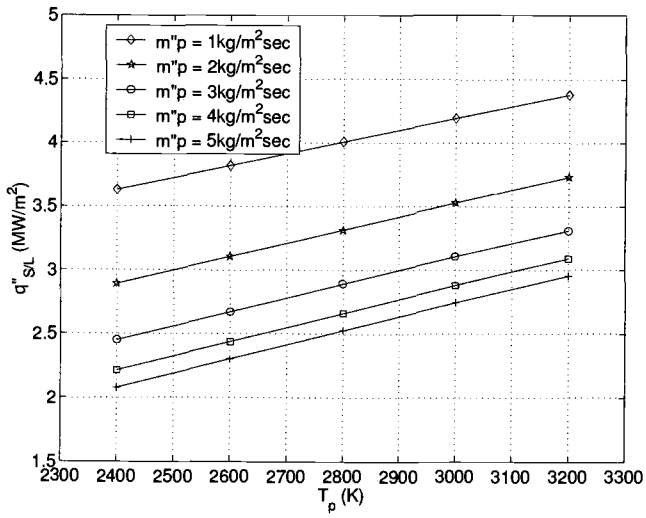

Figure 6.17. Effect of particle temperature on the solid/liquid alumina interface heat flux for $q''_{gas} = 3MW/m^2$ at time $t = 5s$.

6.5. Heat flux to the ablative surface

Figure 6.18 presents the variation in the heat flux to the ablative surface over time for a particle temperature $T_p = 2800$ K and a gas heat flux $q''_{gas} = 3MW/m^2$. It can be observed from the graph that the heat flux to the ablative surface decreases with the development of the alumina. During the initial phase, the ablative surface

is exposed to very high heat flux but as the alumina builds up on the ablative surface, the heat flux decreases drastically to values below $5MW/m^2$ and becomes nearly asymptotic with time. This shows that the alumina particles, although, they imposes a high heat flux during the initial phase, as time proceeds begins to protect the ablative surface from high thermal loading. The extent of this protection depends on the thickness of the alumina and hence a higher mass flux of alumina particles tends to shield the ablative surface more effectively.

The heat flux to the ablative surface for a particle mass flux of $1kg/m^2s$ is reduced by 39%, over a time period of $5s$, by the development of the alumina. Increasing particle mass flux to $5kg/m^2s$, the heat flux to the ablative surface is reduced by 88% over the time period of $5s$. For this mass flux during the early phase of development where only the solid layer exists, the heat flux is reduced by 25%. But as soon as the alumina enters the later phase of the development, where both the solid and the liquid alumina layers co-exist, the heat flux to the ablative surface is reduced by 66%. Figure 6.18 also shows that the thicker liquid alumina layer, which is a result of higher mass flux as shown in Fig. 6.10, offers more thermal resistance than the solid layer. This is evident from the slope change in Fig. 6.18 when liquid alumina layer starts growing. This can be attributed to two effects. One, there is a decrease in the thermal conductivity for the liquid upto 38% due to the temperature variations in the liquid region from 2400 K to 4200 K. Second, the thickness of the liquid layer becomes greater than the solid layer with higher particle mass flux cases having a higher thickness. Figure 6.19 shows the ablative heat flux in a log-log plot. The plot clearly shows the transition, by changing the slope of the curves, where both solid and liquid alumina layers begin to co-exist.

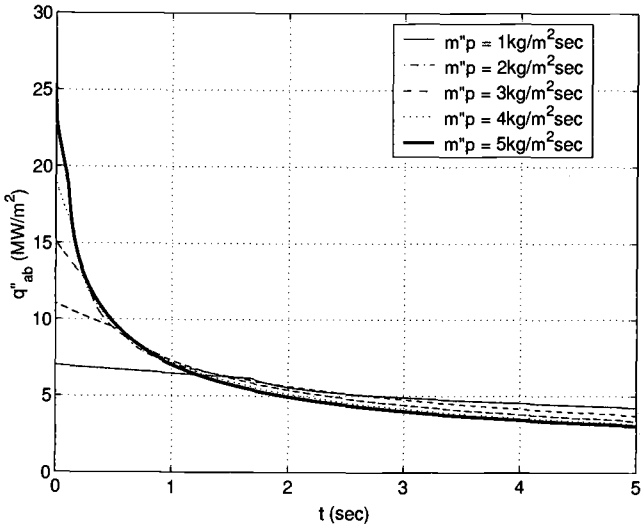

Figure 6.18. Variation of heat flux to the ablative surface for $T_p = 2800$ K and gas heat flux of $q''_{gas} = 3MW/m^2$.

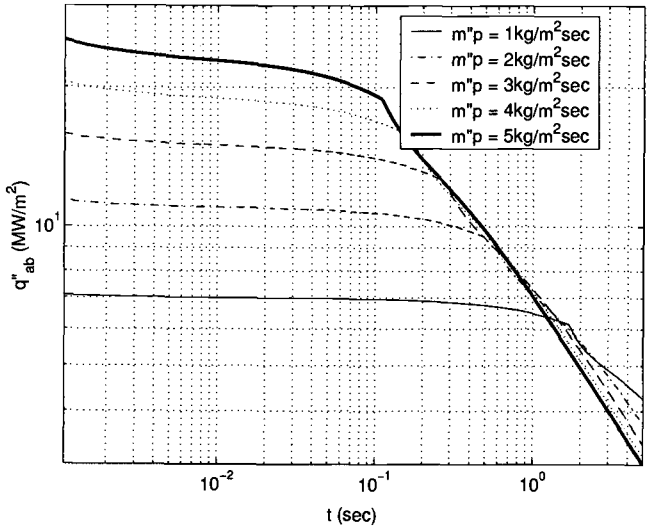

Figure 6.19. Variation of heat flux to the ablative surface for $T_p = 2800$ K and gas heat flux of $q''_{gas} = 3MW/m^2$ in the log-log plot.

6.5.1. Effect of gas heat flux on the heat flux to the ablative surface

The effect of the gas heat flux on the energy transferred to the ablative surface is presented in Fig. 6.20 for a particle temperature $T_p = 2800$ K at time $t = 5s$. It can be observed from this graph that as the gas heat flux increases the heat flux to the ablative surface also increases, essentially linearly. But for higher mass fluxes the rate of this increase is less due to thicker liquid alumina layer. An example, 21% of the $11MW/m^2$ gas heat flux supplied to the top surface does not reach the ablative surface for a mass flux of $1kg/m^2s$ versus 64% of the $11MW/m^2$ supplied gas heat flux for a mass flux of $5kg/m^2s$.

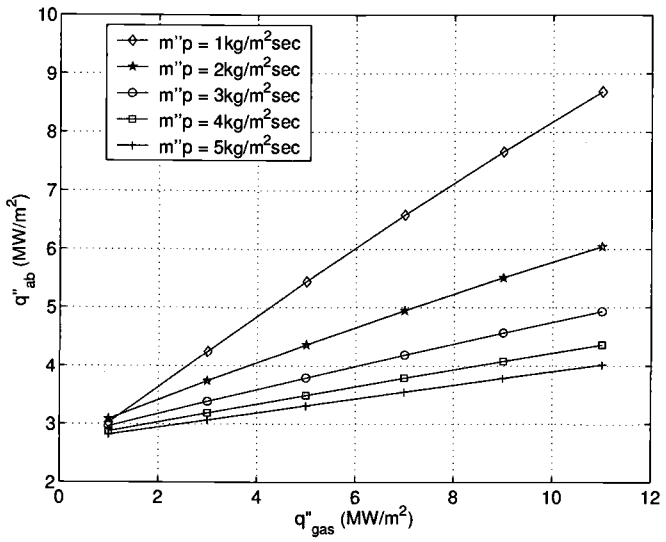

Figure 6.20. Effect of gas heat flux on the heat flux to the ablative surface for a particle temperature $T_p = 2800$ K at time $t = 5s$.

6.5.2. Effect of particle temperature on the heat flux to the ablative surface

The effect of the particle temperature on the energy transferred to the ablative surface is presented in Fig. 6.21 for a gas heat flux of $q''_{gas} = 3MW/m^2$ at time $t = 5s$. Figure 6.21 shows that the heat flux to the ablative surface linearly increases with the particle temperature. The slope is not affected by the mass flux, but the temperatures are significantly lower for higher values of mass flux. This linear effects can be attributed to the direct addition of particle energy to the alumina instead of applying it through a boundary condition.

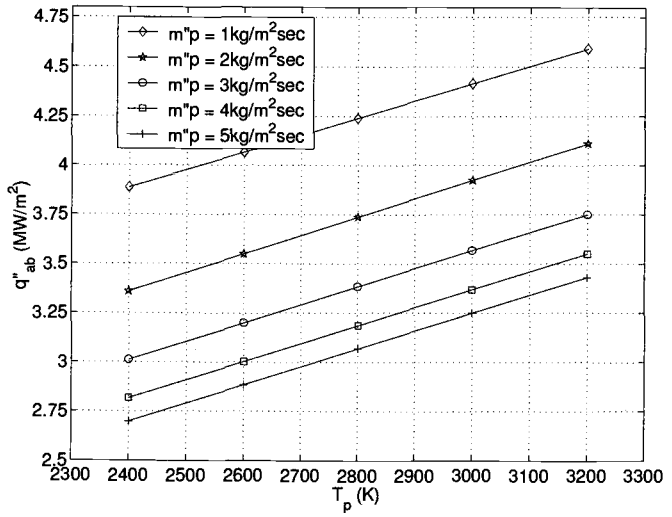

Figure 6.21. Effect of particle temperature on the heat flux to the ablative surface for a gas heat flux $q''_{gas} = 3MW/m^2$ K at time $t = 5s$.

6.6. Discussion

A total of 50 cases were studied and the results for the base case are presented in the previous sections. The effect of the particle mass flux, gas heat flux and particle temperature on the solidification dynamics and heat transfer characteristics were presented, and it is found that the mass flux of the particles is the major factor affecting the growth rate of solid and liquid alumina layer and the energy transferred to the ablative suraface. The thermal resistance of the alumina increases with the increase in the mass flux due to an increase in the thickness of alumina. Hence a high particle mass flux is characterized by a very high initial thermal loading but offers maximum protection in the later stages of alumina development. High thermal loading is nothing but high heat transfer rate to the ablative surface, which can be observed for the higher mass fluxes in Fig. 6.18. The presence of the alumina on the ablative surface decreases the energy transferred to the ablative surface by approximately 39% to 88%, depending on the particle mass flux in the range $1kg/m^2s$ to $5kg/m^2s$.

The effects of the temperature dependence of the thermo-physical properties of alumina were studied in the Chapter 4. The thermal conductivity varies by as much as 65% within the operating temperature range presented. This variation directly affects the thermal resistance of the alumina and causes the temperature of the alumina to increase. For the base case conditions and a mass flux of $1kg/m^2s$, presented in Fig. 4.8, the variation in the temperature distribution is approximately 13%. This study shows the importance of accounting for the variable thermo-physical properties of the alumina.

In Chapter 5 the computational model was partially verified using an analytical Stefan solution and it was found that the computational model agrees well with the analytical solution, with approximately 0.02% error in the temperature between the analytical solution and predicted numerical solution.

A closer look at the effect of the mass flux reveals that the mass flux has more significant impact when variations occurs from lower values of mass flux such as from $1kg/m^2s$ to $2kg/m^2s$ verses increasing the mass flux from $2kg/m^2s$ to $4kg/m^2s$. In this study increasing the mass flux from $1kg/m^2s$ to $2kg/m^2s$ causes the relative solid thickness to decrease from 48% to 27%. On the other hand increasing the mass flux from $2kg/m^2s$ to $4kg/m^2s$ causes the solid thickness ratio to decrease from 27% to 20% as observed in Fig. 6.9. Thus having a higher mass flux is found to have a lesser effect on the solidification dynamics of alumina.

An increase in the particle temperature has a linear effect on the solidification dynamics of alumina which includes the solid and liquid alumina layer growth. Also, the particle temperature effects are approximately linear for the heat transfer characteristics of the alumina. For example, in Fig. 6.21 the slope of the curves are not affected by the mass flux which is an indication of the existence of a linear relationship for the particle effects.

In general, the higher the gas heat flux the lower the solid layer thickness and the higher the energy transferred to the ablative surface. But the effect of the gas heat flux also depends on the mass flux of the particles. The gas heat flux has a major effect only for lower mass fluxes compared to higher mass fluxes. A higher mass flux develops a thicker alumina which in turn has a higher thermal resistance and hence offers maximum protection against thermal loading.

The computational model for this study was developed to help study the heat transfer characteristics of the vertical missile launch systems. Experimental data from the missile launch systems is required to validate this computational model. A closer look at the computational model reveals that a constant heat flux boundary condition, or the Neumann boundary condition, was used to study the heat transfer characteristics. But in an actual system the gas flow over the ablative surface imposes a convective boundary condition, or a mixed thermal boundary condition. To use the mixed boundary condition instead of the Neumann boundary condition, the properties and the conditions prevailing in the exhaust gas have to be known accurately. Due to the complexity involved in the high speed supersonic flow, the convective effects of the exhaust gas was neglected. The use of the Neumann boundary condition instead of the mixed boundary condition causes the temperature of the alumina to rise to very high values, which might not be the case if a mixed boundary condition was used.

Inspite of this limitation of the model boundary condition, the Neumann boundary condition is justified for studying the heat transfer characteristics in the early stages of the alumina formation. This is because the surface temperature of the alumina is much lower than the gas temperature resulting in a high heat transfer rate equivalent to a Neumann boundary condition. The Neumann boundary condition is also justifyable in situations where the radiation heat effects are high and also in case of high mass fluxes where the particle kinetic energy is high enough to impose a constant heat flux boundary condition. Whether a constant heat flux boundary condition is used or a mixed boundary condition is used, the effect of the alumina

is to protect the ablative surface, which is evident from the results presented in the previous sections.

The flow characteristics of the exhaust gas was investigated by Lewis and Anderson [2]. In their work it was reported that the exhaust gas forms a characteristic recirculation region, near the stagnation point, having low shear stress values inside the region. In this region the alumina will not be smeared due to the low shearing rate imposed by the exhaust gas. Hence the computational model developed in this research will more accurately predict the effects of the alumina in this region because the model assumes that the alumina is not convected. The amount of particles entering this stagnation region depends on the size distribution of the particles. It was reported in the previous study [2], that only small size particles are carried along the gas flow path, where as the heavier particles impinge inside this stagnation region. Hence the predicted results of the computational model will be close to the experimental results if the particle distribution consists of larger size particles. In this region liquid and solid alumina layers tend to grow simultaneously as predicted in the model. The computational model can be extended to predict the heat transfer characteristics away from the stagnation region but with some error, which can only be found using experimental data.

The ultimate goal of the computational model is to develop a more accurate heat transfer model of the alumina and predict the heat flow into the ablative surface. Whether the ablative layer will be able to protect the missile launch system in the event of launch failure from the serve thermal loading, can further be investigated using the predicted results of this model. The results presented in the previous sections shows that the energy transferred to the ablative surface becomes

approximately asymptotic during the later phase of the alumina layer development. Hence in the event of a launch failure the ablative surface should be able to with stand this heat flux for the full burn time of the missile motor. The magnitude of this heat flux depends on the particle mass flux and the gas heat flux.

7. CONCLUSIONS AND RECOMMENDATIONS

A more accurate heat transfer model of the alumina layer was developed to study the solidification dynamics of alumina. The model also helped to predict the heat transferred to the ablative surface. The effects of the thermal loading, particle loading and temperature dependence of the thermo-physical properties of alumina were analyzed in this investigation. The computational model was partially verified using an analytical solution to the Stefan problem. To further validate the computational model experimental data are required.

It can be concluded that the particle mass flux is the major factor affecting the solidification growth rate of alumina and the development of the liquid alumina layer. However, the effect of the gas heat flux was found to have a major effect on the solidification dynamics for the lower mass fluxes. As the mass flux increases to higher values, the thermal resistance of the alumina layer also increases and helps to reduce the influence of the gas flux effectively. The particle temperature has a linear effect on the solid layer growth rate.

Particle mass flux was found to have a major effect on the initial thermal loading on the ablative surface. The higher the particle mass flux, the higher was the heat transferred to the ablative surface during the early phase of alumina layer development. But in the later phase, the heat transferred to the surface is reduced drastically to lower values which is attributed to the very thin layer of alumina that exists during the initial phase of development. But for higher mass fluxes the gas heat flux was effectively shielded, which can be attributed to the increase in the thermal resistance of the alumina layer with mass flux. The heat transferred to the ablative surface was reduced roughly by 39% to 88% for a mass flux varying from $1 kg/m^2 s$

to $5kg/m^2s$. Similar to the solidification dynamics, the particle temperature has only a linear effect on the heat transferred to the ablative surface. The effects of the temperature dependence of the thermo-physical properties of alumina were analyzed and found to have a reasonable effect that cannot be neglected.

Recommendations for future research include incorporating the convective effects of the liquid alumina layer due to smearing action of the exhaust gas flow. This will make the model more complete and accurate in predicting the heat transfer characteristics of alumina layers in all the regions of gas flow. One way to do this is to combine the present model with the CRAFT code [12], which is a fully coupled multi-phase 1D/2D/AXI/3D Navier Stokes flow solver. The CRAFT code provides all the information required to apply the convective boundary condition at the alumina surface. Modification to the present model will require to extend it to two-dimension.

Developing an ablation model for the ablative surface, which will take into consideration the mechanical erosion, and coupling it along with this computational model will not only help improve the design of the current vertical launch system, but also help to validate the computational model. This is because it is more feasible to get erosion data from missile launches compared to getting heat flux data in the high temperature environment.

BIBLIOGRAPHY

[1] John Crank., *Free and Moving Boundary Problems*, 1984, Clarendon Press, Oxford.

[2] Lewis, D. J., and Anderson L. P., "Effects of Melt-Layer Formation on Ablative Materials Exposed to Highly Aluminized Rocket Motor Plumes", *36th Aerospace Sciences Meeting and Exhibit*, Reno, NV, Jan. 1998.

[3] Ungar, E. W.,"Particle Impacts on the Melt Layer of an Ablating Body", *ARS Journal*, Vol. 30, No. 9, Sept. 1960, pp. 799-805.

[4] Soo Hoo, G., *Predictions of the Plenum Floor Erosion in the Vertical Launching System from a Mk 104 Dual-Thrust Rocket Motor Restrained Firing*, NSWC TR-84-265, April 1995.

[5] Yang, B. C., Cheung, F. B., and Koo, J. H., "Numerical Investigation of Thermo-Chemical and Mechanical Erosion of Ablative Materials", *AIAA/SAE/ASME/ASEE 29th Joint Propulsion Conference and Exhibit*, Monterey, CA, June 28-30, 1993.

[6] Yang, B. C., Cheung, F. B., and Koo, J. H., "Modeling of One-Dimensional Thermo-Mechanical Erosion of High-temperatur Ablatives", *Journal of Applied Mechanics*, Vol. 60, Dec. 1993, pp. 1027-1032.

[7] Cheung, F. B., Yang, B. C., Burch, R. L., and Koo, J. H., "Effect of Melt Layer Formation on Thermo-Mechanical Erosion of High-temperature Ablative Materials" *Proceedings of Pacific International Conference on Aerospace Science and Technology*, National Cheng Kung University, Taiwan, 1993, pp. 302-309.

[8] Crank, J., "Moving Boundary Problems in Diffusion and Heat Flow", *Q. Jl. Mech. appl. Math.*, Vol. 10, 1957, pp. 220-231.

[9] Douglas, J. and Gallie, J. M.,"On the Numerical Integration of a Parabolic Differential Equation Subject to a Moving Boundary Condition" *Duke Math. J.*, , Vol. 22, 1955, pp. 557-571.

[10] Gupta, R. S., and Kumar, D., "Variable Time Step Methods for One-Dimensional Stefan Problem with Mixed Boundary Condition" *Int. J. Heat Mass Transfer*, Vol. 24, 1981, pp. 251-259.

[11] Murray, W. D., and Landis, F., "Numerical and Machine Solutions of Transient Heat-Conduction Problems Involving Melting or Freezing", *Journal of heat Transfer, Trans. ASME* (c) 81, pp. 106-112.

[12] Sinha, N., Dash, S. M.., and Hosangadi, A., "Applications of an Implicit, Upwind NS Code, CRAFT, to Steady/Unsteady Reacting, Multi-Phase Jet/Plume Flowfields," *AIAA-92-0837, AIAA Aerospace Sciences Meeting,* Jan. 6-9, 1992.

[13] Versteeg, H.K. and Malalasekera, W., *An Introduction to Computational Fluid Dynamics: The Finite Volume Method,* 1995, Prentice Hall, Harlow:England.

[14] Patankar, S.V., *Numerical Heat Transfer and Fluid Flow,* 1980, Hemisphere Publishing, New York.

[15] Incopera, F. P. and DeWitt, D. P., *Fundamentals of Heat and Mass Transfer* , 1996, John Wiley and Sons, New York.

[16] *Guide for the Verification and Validation of Computational Fluid Dynamics Simulations,* American Institute of Aeronautics and Astronautics, 1998.

[17] *Material Properties Package Reference Manual,* Sandia National Laboratory.

APPENDICES

```
c.....FORTRAN Program to Study the Solidification Dynamics with
      Liquid Mass Influx
c.....
c     Mass flux = 1kg/m^2s
c     Heat flux = 3 MW/m^2
c     Particle temperature = 2400 K
c.....
      Program Solidification
      implicit none
      integer i,j,n_node,n_volume,r,m
      integer flag,flag1,z
      real(kind = 8) rho,Latent,ko,cpo,alpha,d,Vp
      real(kind = 8) Ta,Ti,Tp,T_fusion,flux,Fluxn,mp,KEE,dt
      real(kind = 8) To(5000),X(5000)
      real(kind = 8) cp(5000),k(5000)
      real(kind = 8) dx_s,dt_s,L_ref,L_iref,L_oref,Time_ref,Time_s,Time
      real(kind = 8) Ta_s,Ti_s,Tp_s,T_fusion_s,T_expo
      real(kind = 8) kr,Tr2,Tr3,Tr4
      real(kind = 8) Ablative_heat,Interface_heatflux
      real(kind = 8) New_mass,Total_mass
      real(kind = 8) p,solid_L,Iminus,Iplus
      real(kind = 8) ae(5000),aw(5000),ap(5000),b(5000)
      real(kind = 8) ke,kw,Su,Sp,apo,c1,c2,temp1,dis
      real(kind = 8) time_begin,time_end
```

```
      CALL CPU_TIME(time_begin)
c.....Properties of Alumina at 1600 k (reference temperature)
      rho = 4000.0D+00       !kg/m3
      cpo = 1310.0D+00       !j/kg k
      Latent = 1.07D+06      !j/kg
      ko = 4.07D+00          !w/m k
      alpha = ko/(rho*cpo)   !m2/s
c.....Boundary Conditions
c.....Bottom Wall Temperature
      Ta = 1600.0D+00        !k
      Ti = 2400.0D+00        !k
      Tp = 2400.0D+00        !k
      T_fusion = 2327.0D+00 !k
c.....Mass flowrate of particle
      mp = 1.0D+00           !kg/m2 s
      Vp = 1650.0D+00        !m/s
c.....Heat flux on Top Alumina Layer with Particle Kinetic Energy
      KEE = mp*Vp**2.0/2.0   !W/m2
      Flux = 3.0D+06 + KEE   !W/m2
c.....Diffusion Number
      d = 1.0D-2
c.....Non-Dimensional temperature
      Ta_s = 0.0D+00
      Ti_s = 1.0D+00
```

```
      Tp_s = 1.0D+00
      T_fusion_s = (T_fusion-Ta)/(Tp-Ta)
c.....Reference Length & Time
      L_iref = (mp/rho)*5.0D+00     !m
      Time_ref = L_iref**2/alpha    !s
c.....Initial Time step
      dt = 1.0D-3                   !s
      Time_s = dt/Time_ref
c.....Number of Volumes and Node
      n_volume = 500
      n_node = n_volume + 1
c.....Time Step & Space Step
      dx_s = 1.0D+00/n_volume
      dt_s = dx_s**2*d      ! (d=a*dt/dx^2)
c.....Initial Condition and Boundary Condition
      To(1) = Ta_s
      do i = 2,n_node
         To(i) = Ta_s
      enddo
c.....Files for Storing the Results
c.....Stores the varition of the Temperature with Time
      open(60,file = 'Temp_DisT.txt',status = 'unknown')
      open(50,file = 'Temp_DisX.txt',status = 'unknown')
c.....Stores the location of the Solid/Liquid Interface with Time
```

```
      open(110,file = 'SL_Interface_X.txt',status = 'unknown')
      open(120,file = 'SL_Interface_t.txt',status = 'unknown')
c.....Stores the Ablative Layer Heat Flux Variation with Time
      open(11,file = 'AB_heatflux.txt',status = 'unknown')
      open(12,file = 'AB_heatflux_t.txt',status = 'unknown')
c.....Stores the Solid/Liquid Interface Heat Flux Variation with Time
      open(70,file = 'SL_heatflux.txt',status = 'unknown')
      open(80,file = 'SL_heatflux_t.txt',status = 'unknown')
c.....Stores the Surface Temperature Variation with Time
      open(90,file = 'Surf_Temp.txt',status = 'unknown')
      open(100,file = 'Surf_Temp_t.txt',status = 'unknown')
c.....Stores the Ratio of the Solid Layer Thickness to the Total Thickness
      open(130,file = 'Solid_ratio.txt',status = 'unknown')
      open(140,file = 'Solid_ratio_t.txt',status = 'unknown')
c.....Stores the Ratio of the Melt Layer Thickness to the Total Thickness
      open(150,file = 'melt_ratio.txt',status = 'unknown')
      open(160,file = 'melt_ratio_t.txt',status = 'unknown')
c.....Stores the Final Temperature Distribution
      open(170,file = 'F_Temp_Dis_T.txt',status = 'unknown')
      open(180,file = 'F_Temp_Dis_X.txt',status = 'unknown')
c....Initialization of Variables
      r = 0
      j = 100
      m = 1
```

```
      flag = 0
      flag1 = 0
      Time = 1
ccccccccccccccccccccccccccccccccccccccccccccccccccccccccc
c..... Time Loop
ccccccccccccccccccccccccccccccccccccccccccccccccccccccccc
c
c.....Time Loop
      do while (time_s .LE. 5.0/Time_ref)

         Time_s = Time_s + dt_s
         L_oref = L_ref
c.....Reference Length Calculated for Each Time Step
         L_ref = (mp/rho)*time_s*Time_ref      !m
c.....Mass Deposited in Each Time Step
         New_mass = mp*dt_s*Time_ref/(L_ref*rho)
         Total_mass = dx_s
c.....Volume Averaged Temperature for the End Node to
c     Account for the Thermal Energy of the Particles
         To(n_node) = New_mass*Ti_s/Total_mass +
     $        (dx_s-New_mass)*To(n_node)/Total_mass
c.....Manually Locating the Moving Interface
         if (flag1 .EQ. 0) then
            i = 1
```

```
            do while (To(i) .LT. T_fusion_s)
               r = i+1
               i = i+1
               if (i .EQ. n_node) goto 20
            enddo
 20         p = 1 + (T_fusion_s - To(r-1))/(To(r) - To(r-1))
            r = r-1
         endif
c.....calculating the Variable Thermal Conductivity
         if (j .EQ. 100) then
            call conductivity(To,n_node,k)
         endif
c.....calculating the Variable Specificheat Capacity
         if (j .EQ. 100) then
            call Specificheat(To,n_node,cp)
            j = 1
         endif
         j = j+1
c.....Tracking the Solid/Liquid Interface using lagrangian Interpolation
         if (r .GT. 5 .AND. r .LT. n_node-5) then
            flag1 = 1
c.....Calculating the Amount of Solid formed in One Time Step
 10         call growth(To,k,Latent,dx_s,dt_s,L_oref,L_iref,r,p)
c.....Mapping the Solid/Liquid Interface Location to the New Grid
```

```
            solid_L = ((r-2)*dx_s + p*dx_s)*L_oref
            p = (solid_L - (r-2)*dx_s*L_ref)/(dx_s*L_ref)
c.....Incrementing the Reference Node for the Solid/Liquid Interface
            if (p .GE. 2.0) then
               p = 1.001D+00
               r = r+1
c.....If the Entire Melt Layer Becomes Solid the Interace Boundary
c.....Condition is Not Applied
               if (r .GE. n_node-5) then
                  flag1 = 0
                  print*, "rn-5"
                  goto 100
               endif
               flag = 1
            endif
c.....Decrementing the Reference Node for the Solid/Liquid Interface
            if (p .LE. 1.0) then
               p = 1.999D+00
               r = r-1
c.....If the Entire Melt Layer Becomes Liquid the Interace Boundary
c     Condition is Not Applied
               if (r .LE. 5) then
                  flag1 = 0
                  print*, "r5"
```

```
                goto 100
              endif
              flag = 1
            endif
c.....Calculating the Amount of Solid Between the Reference Node and the
c     Solid/Liquid Interface
          Iminus = (p-1)*dx_s
c.....Calculating the Amount of Liquid Between the Reference Node and the
c     Solid/Liquid Interface
           Iplus = (2-p)*dx_s
        endif
c-------------------------------------------------------
c.....              Space Loop
c-------------------------------------------------------
 100    do i = 2,n_node
c.....Harmonic Mean of the Thermal Conductivities
           kw = 2*k(i)*k(i-1)/(k(i) + k(i-1))
           if (i .EQ. n_node) then
              k(i+1) = k(i)
           endif
           ke = 2*k(i)*k(i+1)/(k(i) + k(i+1))
c.....Coefficients
           c1 = L_iref**2/(L_ref**2*dx_s)
           c2 = 1.0/time_s
```

```
c.....Coefficients for the Nodes Between the Boundaries
            if (i .NE. 2 .AND. i .NE. n_node) then
               aw(i) = c1*kw-(c2*cp(i-1)*((i-2)*dx_s-dx_s/2.0)/2.0)
               ae(i) = c1*ke+(c2*cp(i+1)*(i*dx_s-dx_s/2.0)/2.0)
            endif
            apo = cp(i)*dx_s/dt_s
            Su = 0.0
            Sp = 0.0
            b(i) =  apo*To(i) + Su
            ap(i) = c1*ke + c1*kw + c2*cp(i)*dx_s + apo -Sp
c......Constant Wall Temperature Boundary Condition
            if(i .EQ. 2) then
               aw(i) = 0.0
               ae(i) = c1*ke+(c2*cp(i+1)*(i*dx_s-dx_s/2.0)/2.0)
               apo = cp(i)*dx_s/dt_s
               sp = -2.0*c1*kw
               Su = 2.0*c1*kw*Ta_s
               b(i) =  apo*To(i) + Su
               ap(i) = c1*ke + c2*cp(i)*dx_s -
     $              c2*cp(i)*((i-1)*dx_s-dx_s/2.0)/2.0 + apo -Sp
            endif
c.....Interface Boundary Condition
           if (flag1 .EQ. 1) then
              if (i .EQ. r) then
```

```
                ae(i) = 0.0
                apo = cp(i)*(dx_s/2.0 + Iminus)/dt_s
                Sp = -c1*dx_s*ke/Iminus
                Su = c1*dx_s*ke*T_fusion_s/Iminus +  c2*1.0558D+00
     $             *((i-2)*dx_s+dx_s/2+Iminus)*T_fusion_s!1.0558
                b(i) =  apo*To(i) + Su
                ap(i) = c1*kw + c2*cp(i)*dx_s +
     $               c2*cp(i)*((i-1)*dx_s-dx_s/2.0)/2.0 + apo -Sp
              endif
             if (i .EQ. r+1) then
                aw(i) = 0.0
                apo = cp(i)*(dx_s/2.0 + Iplus)/dt_s
                Sp = -c1*dx_s*kw/Iplus
                Su = c1*dx_s*kw*T_fusion_s/Iplus - c2*1.0846D+00
     $              *((i-3)*dx_s+dx_s/2+Iminus)*T_fusion_s!1.0846
               b(i) =  apo*To(i) + Su
               ap(i) = c1*ke + c2*cp(i)*dx_s -
     $               c2*cp(i)*((i-1)*dx_s-dx_s/2.0)/2.0 + apo -Sp
              endif
           endif
c....Solidification Heat Added along with the Heat Flux when the
c    Solid Layer Alone Grows
            Fluxn = Flux
            if (flag1 .NE. 1) then
```

```
              Fluxn = Flux + latent*mp
            endif
c.....Constant Heat Flux  Boundary Condition
            if(i .EQ. n_node) then
               ae(i) = 0.0
               aw(i) = c1*kw-(c2*cp(i-1)*((i-2)*dx_s-dx_s/2.0)/2.0)
               apo = cp(i)*dx_s/dt_s
               sp = 0.0
               T_expo  = 1.5*(To(n_node)-To(n_node-1))+To(n_node-1)
               Su = c1*dx_s*Fluxn*L_ref/(ko*(Tp-Ta))+c2*cp(i)*T_expo
               b(i) = apo*To(i) + Su
               ap(i) = c1*kw + c2*cp(i)*dx_s +
     $              c2*cp(i)*((i-1)*dx_s-dx_s/2.0)/2.0+ apo -Sp
            endif
         enddo
c.....End of Space Loop
c-------------------------------------------------------------
c.....calling the TDMA solver to Find the Temperature Distribution
         call tridiag(aw,ae,ap,b,n_node,To)
c....Storing the Temperature Distribution Variation
         if (Time-Time_s*Time_ref .LE. 1.0e-3) then
            print*, Time_s*Time_ref-time
            do i = 1,n_node
               write(60,*) (To(i)*(Tp-Ta)+Ta)
```

```
            enddo
c.....Grid generation
            dis = -dx_s/2.0
            do i = 1,n_node
               X(i) = dis
               dis = dis + dx_s
            enddo
c.....Writing the Grid
            do i = 1,n_node
               write(50,*) X(i)*L_ref
            enddo
            Time = Time+1
c.....Storing the Surface Temperature
            write(90,*) To(n_node)*(Tp-Ta)+Ta
            write(100,*) Time_s*Time_ref
         endif
c.....Storing the Solid/Liquid Interface Position
         if (flag1 .EQ. 1 .AND. m .EQ. 1000) then
            write(110,*) (r-2.5+p)*dx_s*L_ref
            write(120,*) time_s*Time_ref
         endif
c.....Storing the Heat Flux to the Ablative layer
         if (m .EQ. 1000) then
            Ablative_heat = (k(1)+k(2))*ko*To(2)*(Tp-Ta)/
```

```
     $           (dx_s*L_ref)
                 write(11,*) Ablative_heat
                 write(12,*) Time_s*Time_ref
              endif
c.....Storing the Heat Flux to the Ablative layer S/L Interface
              if (flag1 .EQ. 1 .AND. flag .EQ. 1) then
                 kr = (k(r+2)+k(r+3)+k(r+4))/3.0
                 Tr2 = To(r+2)*(Tp-Ta)+Ta
                 Tr3 = To(r+3)*(Tp-Ta)+Ta
                 Tr4 = To(r+4)*(Tp-Ta)+Ta
                 Interface_heatFlux = kr*ko*(-1.5*Tr2 +
     $           2.0*Tr3 - 0.5*Tr4)/(dx_s*L_ref)
                 write(70,*) Interface_heatFlux
                 write(80,*) Time_s*Time_ref
              endif
c.....Storing the Ratio of the Solid Layer Thickness to the Total Thickness
              if (flag1 .EQ. 1 .AND. m .EQ. 1000) then
                 write(130,*) (r-2.5+p)/(n_node-1)
                 write(140,*) time_s*Time_ref
              endif
c.....Storing the Ratio of the Melt Layer Thickness to the Total Thickness
              if (flag1 .EQ. 1 .AND. m .EQ. 1000) then
                 write(150,*) ((n_node-1)-(r-2.5+p))/(n_node-1)
                 write(160,*) time_s*Time_ref
```

```
            endif
            if (m .GE. 1000) m = 0
            flag = 0
            m = m+1
         enddo
c.....End of Time Loop
ccccccccccccccccccccccccccccccccccccccccccccccccccccccccccccccccccc
c.....Closing the Output Files
         close(11)
         close(12)
         close(50)
         close(60)
         close(70)
         close(80)
         close(90)
         close(100)
         close(110)
         close(120)
         close(130)
         close(140)
         close(150)
         close(160)
c.....Grid generation
         dis = -dx_s/2.0
```

```
      do i = 1,n_node
         X(i) = dis
         dis = dis + dx_s
      enddo
c.....Writing the Grid
      do i = 1,n_node
         write(180,*) X(i)*L_ref
      enddo
c.....Writing the Final Temperature Distribution
      do i = 1,n_node
         write(170,*) (To(i)*(Tp-Ta)+Ta)
      enddo
      close(170)
      close(180)
      CALL CPU_TIME(time_end)
      print*, 'Time of operation ', time_end - time_begin, ' seconds'
      print*,''
      print*, 'solid thickness',(r-2.5+p)*dx_s*L_ref
      print*,''
      print*, 'Surface Temperature',To(n_node)*(Tp-Ta)+Ta
      print*,''
      print*, 'S/L Interface Position',(r-2.5+p)*dx_s*L_ref
      print*,''
      print*, 'Ablative_heat',Ablative_heat
```

```
      print*,''
      print*, 'Interface_heatFlux',Interface_heatFlux
      print*,''
      print*, 'Solid ratio',(r-2.5+p)/(n_node-1)
      print*, ''
      print*, 'Liquid ratio',((n_node-1)-(r-2.5+p))/(n_node-1)
      stop
      end
c.....End of Main Program
c^^^^^^^^^^^^^^^^^^^^^^^^^^^^^^^^^^^^^^^^^^^^^^^^^^^^^^^^^^^^^^^


c##############################################################
c
c                      SUBROUTINES
c
c##############################################################

c^^^^^^^^^^^^^^^^^^^^^^^^^^^^^^^^^^^^^^^^^^^^^^^^^^^
c     Tridiagonal Matrix Solver
c^^^^^^^^^^^^^^^^^^^^^^^^^^^^^^^^^^^^^^^^^^^^^^^^^^^
      subroutine tridiag(aw,ae,ap,b,n_node,Ans)
      implicit none
```

```
      integer i,n_node
      real(kind = 8) aw(5000),ae(5000),ap(5000),b(5000)
      real(kind = 8) alpha,beta,D,C,C1(5000),A(5000),Ans(5000)
      A(1) = 0.0
      C1(1) = 0.0
c..... Forward Elimination
      do i = 2,n_node
         beta = aw(i)
         D = ap(i)
         alpha = ae(i)
         C = b(i)
         A(i) = Alpha/(D - beta*A(i-1))
         C1(i) = (beta*C1(i-1) + C)/(D - beta*A(i-1))
      enddo
c.....Backward Substitution
      do i =  n_node,2,-1
         Ans(i) = A(i) *Ans(i+1) + C1(i)
      enddo
      return
      stop
      end

c^^^^^^^^^^^^^^^^^^^^^^^^^^^^^^^^^^^^^^^^^^^^^^^^^^^^^^^^^^^^^^^^^^^^^^^^^^^^
c        Calculating the Variable Thermal Conductivity
```

```
c^^^^^^^^^^^^^^^^^^^^^^^^^^^^^^^^^^^^^^^^^^^^^^^^^^^^^^^^^^^^^^^^^^^^^^^^^^^^
      subroutine conductivity(T,n_node,k)
      implicit none
      integer i,n_node
      real(kind = 8) p,q,T(5000),k(5000),Tp,Ta
c.....Reference Temperatures
      Tp = 2400D+00
      Ta = 1600D+00
c.....Coefficients for Calcualting Variable Thermal Conductivity
      p = 2375.44619278885D+00
      q = -0.86327184617D+00
      do i = 1,n_node
         k(i) = (p*(T(i)*(Tp-Ta)+Ta)**q)/4.07
      enddo
      return
      stop
      end

c^^^^^^^^^^^^^^^^^^^^^^^^^^^^^^^^^^^^^^^^^^^^^^^^^^^^^^^^^^^^^^^^^^^^^^^^^^^^
c     Calculating the Variable Specific Heat Capacity
c^^^^^^^^^^^^^^^^^^^^^^^^^^^^^^^^^^^^^^^^^^^^^^^^^^^^^^^^^^^^^^^^^^^^^^^^^^^^
      subroutine Specificheat(T,n_node,cp)
      implicit none
      integer i,n_node
```

```
      real(kind = 8) T(5000),cp(5000),p,q,Tp,Ta,cpo
c.....Reference Temperatures
      Tp = 2400D+00
      Ta = 1600D+00
      cpo = 1420.77D+00
c.....Coefficients for Calcualting Variable Specific Heat Capacity
      p = 452.1825743D+00
      q = 0.144147D+00
      do i = 1,n_node
         cp(i) = (p*(T(i)*(Tp-Ta)+Ta)**q)/1310.0D+00
c.....Constant Specific Heat Capacity in the Liquid Region
         if (T(i) .GE. 2327.0D+00) then
            cp(i) = cpo/1310.0D+00
         endif
      enddo
      return
      stop
      end

c^^^^^^^^^^^^^^^^^^^^^^^^^^^^^^^^^^^^^^^^^^^^^^^^^^^^^^^^^^^^^^^^^^^^
c        Subroutine to Locate the Interface
c^^^^^^^^^^^^^^^^^^^^^^^^^^^^^^^^^^^^^^^^^^^^^^^^^^^^^^^^^^^^^^^^^^^^
      subroutine growth(T,k,Latent,dx_s,dt_s,L_oref,L_iref,r,p)
      implicit none
```

```
      integer r
      real(kind = 8) T(5000),k(5000)
      real(kind = 8) p,ks,kl,ki,Cpo,Latent,solidl,liquidl
      real(kind = 8) Tp,Tp_s,Ti,Ta,Coeff
      real(kind = 8) dx_s,dt_s,L_oref,L_nref,L_iref
c.....Reference Temperature
      Tp = 2327.0D+00
      Ti = 2400.0D+00
      Ta = 1600.0D+00
      Cpo = 1310.0D+00
      Tp_s = (Tp-Ta)/(Ti-Ta)
c.....Average Thermal Conductivity for Solid and Liquid
      ki = (2387.16079D+00*Tp**(-0.864098D+00))/4.07D+00
      ks = (k(r-2) + k(r-1) + ki)/3.0
      kl = (ki + k(r+2) + k(r+3))/3.0
c.....Coefficient
      Coeff = Latent*L_oref**2*dx_s**2/((Ti-Ta)*L_iref**2*Cpo*dt_s)
c.....Heat Flux Passing Through the Solid Region
      solidl = (ks/Coeff)*(p*T(r-2)/(p+1) - (p+1)*T(r-1)/p
     $     + (2*p+1)*Tp_s/(p*(p+1)))
c.....Heat Flux from the Liquid Region
      liquidl = (kl/Coeff)*((2*p-7)*Tp_s/((p-3)*(p-4))
     $     + (P-4)*T(r+2)/(p-3) + (p-3)*T(r+3)/(4-p))
c.....Amount of Solidification in One Timestep
```

```
      p = p + solidl - liquidl
      if (T(r+3) .EQ. 0) then
         print*, r,"zero"
         pause
      endif
      return
      stop
      end
c.....End of Subroutines
c###############################################################
```